Piperazine based pH-responsive cyanine dyes for cancer cell photoacoustic imaging

Koki Tsuchiya[†], Hideo Takakura[†], Kohei Nakajima[†], Naoya Ieda[†], Takashi Kaneko[‡], Takeshi Hirasawa[§], Masato Kobayashi[∥,⊥], Yoshihisa Yamaoka[‡], Miya Ishihara[§], Tetsuya Taketsugu[∥,⊥] and Mikako Ogawa[*,†,⊥]

[†]Laboratory of Bioanalysis and Molecular Imaging, Graduate School of Pharmaceutical Sciences, Hokkaido University, Sapporo, Hokkaido, 060-0812, Japan,

[‡]Graduate School of Science and Engineering, Saga University, Saga, Saga, 840-8502, Japan,

[§]Department of Medical Engineering, National Defense Medical College, Tokorozawa, Saitama, 359-8513, Japan,

[∥]Department of Chemistry, Faculty of Science, Hokkaido University, Sapporo, Hokkaido, 060-0810, Japan

[⊥]WPI-ICReDD, Hokkaido University, Sapporo, Hokkaido, 001-0021, Japan

KEYWORDS. photoacoustic imaging, pH, cyanine dyes, activatable probes, cancer

ABSTRACT

Novel pH-responsive Cy7.5 dyes bearing various amino groups were developed for cancer cell photoacoustic (PA) imaging. Among structurally diverse dyes, pH-dependent absorption spectral changes were observed for those carrying a diazaalkyl group. DFT calculations and absorbance measurements of the dyes revealed that these spectral changes depended on the electron density of the pH-sensing moiety. The PA spectra of the dyes also changed pH-dependent fashion and were largely consistent with the absorption spectra. In PA imaging experiments with cultured cancer cells, the pH-responsive dyes conjugated with a cancer specific antibody accumulated in cancer cells and changed their PA signals depending on the acidic lysosome pH. Overall, these results demonstrated that pH-responsive Cy7.5 dyes can be useful for detecting cancer, and the elucidated mechanism of the absorption spectral changes could contribute to designing new PA imaging agents.

1. INTRODUCTION

Dysregulated pH is a hallmark of various diseases, such as cancer, inflammatory diseases, and renal failure [1]. For example, it is widely known that the tumor microenvironment exhibits a mild acidity. Recently, fluorescence dyes responding to abnormal pH levels have gained interest [2,3]. Generally, these dyes bear functional groups that can undergo protonation altering their absorption and fluorescence properties, thus allowing for acidic-environment-selective fluorescence imaging. Based on this principle, Achilefu's group developed cyanine fluorescence dyes for imaging of primary and metastatic breast tumors [4]. In these dyes, protonating the nitrogen atom of the 3*H*-indole moiety is a key step for absorption and fluorescence spectral changes. In another report, Johnsson and Urano's group developed coumarin-hemicyanine hybrid fluorophores and found that the absorption and fluorescence spectra of the dyes change depending on the intramolecular cyclization of the pH-responsive hydroxy, amino, or thiol groups introduced in the 3*H*-indolium moiety [5].

Recently, some researchers applied such a pH-responsive mechanism for developing the new photoacoustic (PA) imaging agents. PA imaging is a novel technique that enables deep tissue imaging since acoustic waves are less scattered and absorbed in biological tissues in contrast to light [6]. PA imaging utilizes the emission of thermal energy from dyes or endogenous absorbers in living body, making it a suitable imaging method for dyes with high absorption coefficient (ε) and low fluorescence quantum yields (φ_f) such as cyanine dyes exemplified by Indocyanine Green (ICG) (ε = 191,000, φ_f = 0.041 in PBS) [7]. Smith's group developed liposomes containing pH-responsive cyanine dyes that change the PA signals by the protonation method of nitrogen atom of 3*H*-indole moiety and achieved deep tissue imaging [8]. Ohe's group developed a novel cyanine derivative for integrin αvβ overexpressing tumor imaging [9]. In this case, the pH-responsive intramolecular cyclization of a thiol moiety was the key step for switching PA signals.

Another pH-responsive mechanism is the introduction of piperazine as a pH-responsive moiety, which has been used in the pH-responsive moieties of various dyes such as rhodamine [10] and naphthalimide [11]. Nagano's group developed cyanine dyes to visualize the weakly acidic tumor microenvironment, which consist of Cy7 dyes and a piperazine ring that serves as a pH-sensing moiety [12]. In this study, we focused on exploiting a piperazin-1-yl group as a pH-responsive moiety of a PA imaging agent. Dyes with absorption in the near-infrared light region are desirable as the excitation light can reach deeper tissue. As dyes meeting these criteria, we selected Cy7.5 analogues having longer conjugation system to show longer wavelength absorption than Cy7 (**Figure 1**), exemplified by ICG (λ_{abs} = 779 nm [7]) and IRDye800CW (λ_{abs} = 785 nm [13]). Various Cy7.5 derivatives with a

piperazin-1-yl group or diverse substituents were synthesized, and their optical properties were compared in this study.

In addition, the pH-responsive mechanism of the piperazine bearing cyanine dyes was investigated. Shifts in absorption spectra, based on the functional group added to the polymethine chain were discussed by Maury's group and Krämer's group [14,15]. The mechanism of the spectral changes of dyes bearing piperazine derivatives, however, remains unclear. Thus, DFT calculations and absorption measurements were performed, highlighting the prominent role of piperazine moieties for switching PA signals. Finally, conjugates of the Cy7.5 derivatives and cancer cell specific antibodies were prepared and applied for pH-responsive PA imaging in cancer cells. These results provided a new platform for designing Cy7.5 PA imaging agents.

2. MATERIAL AND METHODS

2.1. Reagents

Reagents and solvents were purchased from Tokyo Chemical Industry Co. Ltd., (Tokyo, Japan), FUJIFILM Wako Pure Chemicals Corporation (Osaka, Japan), Sigma-Aldrich Co. LLC (St. Louis, MO, USA), Kanto Chemical Co., Inc. (Tokyo, Japan), or Combi-Blocks Inc. (California, USA), and were used without further purification. Reaction solvents were dried on 3Å molecular sieves as needed.

2.2. Synthetic procedure

General synthetic procedure of cyanine dyes with various amino groups: Compound **1** (1 eq.), corresponding amine (3–14 eq.), and NEt_3 (0–123 eq.) were dissolved in anhydrous DMF (0.03–0.20 mL/μmol). The mixture was stirred at 80 ºC under an argon atmosphere. After checking the reaction progress by HPLC, DMF was removed under vacuum and the precipitate was purified by semi-preparative HPLC (A/B = 20 mM NEt_3 in water/99% MeCN, 1% H_2O). After removal of MeCN from the collected fractions, the solution was passed through a cation exchange resin, and then freeze-dried to afford the corresponding cyanine dye.

Preparation of 2: Compound **1** (50.7 mg, 61.7 μmol, see supporting information for synthesis of **1**), piperazine (22.9 mg, 266 μmol), and NEt_3 (50.0 μL, 359 μmol) were dissolved in anhydrous DMF (2 mL). Then, the mixture was reacted and purified according to the general procedure to afford **2** (9.50 mg, 18%) as an orange solid. ^{1}H-NMR (400 MHz, DMSO-d_6): δ 8.19 (d, 2H, J = 9.0 Hz), 7.98 (d, 4H, J = 9.0 Hz), 7.77 (d, 2H, J = 12.0 Hz), 7.69 (d, 2H, J = 9.0 Hz), 7.57 (t, 2H, J = 7.5 Hz), 7.40 (t, 2H, J = 7.5 Hz), 6.11 (d, 2H, J = 12.0 Hz), 4.29 (t,

4H, *J* = 7.0 Hz), 3.75–3.67 (m, 4H), 3.51–3.46 (m, 4H), 3.08–3.02 (m, 4H) , 2.05–1.97 (m, 4H), 1.92 (s, 12H), 1.90–1.83 (m, 4H), 1.80–1.73 (m, 2H). HRMS (ESI$^-$): calcd. for $C_{48}H_{55}N_4O_6S_2$ [M−Na]$^-$ 847.3569, found: 847.3582 (+1.3 mmu).

Preparation of 3: Compound **1** (60.2 mg, 73.3 μmol), 1-methylpiperazine (100 mg, 1.00 mmol) were dissolved in anhydrous DMF. Then, the mixture was reacted and purified according to the general procedure to afford **3** (19.8 mg, 30%) as a red solid. ^{1}H-NMR (400 MHz, DMSO-d_6): δ 8.24 (d, 2H, *J* = 9.0 Hz), 8.02–7.97 (m, 4H), 7.82 (d, 2H, *J* = 14.0 Hz), 7.72 (d, 2H, *J* = 9.0 Hz), 7.58 (t, 2H, *J* = 7.6 Hz), 7.42 (t, 2H, *J* = 7.6 Hz), 6.16 (d, 2H, *J* = 14.0 Hz), 4.32 (t, 4H, *J* = 7.2 Hz), 3.74–3.68 (m, 4H), 3.32–3.28 (m, 4H), 2.57 (t, 8H, *J* = 6.7 Hz), 2.41 (s, 3H), 2.05–1.97 (m, 4H), 1.93 (s, 12H), 1.79–1.72 (m, 2H). HRMS (ESI$^-$): calcd. for $C_{49}H_{57}N_4O_6S_2$ [M−Na]$^-$ 861.3725, found: 861.3742 (+1.7 mmu).

Preparation of 4: Compound **1** (60.3 mg, 73.4 μmol), **S3** (80.0 μL, 454 μmol, see supporting information for synthesis of **S3**), and NEt_3 (40.0 μL, 287 μmol) were dissolved in anhydrous DMF (5 mL). Then, the mixture was reacted and purified according to the general procedure to afford **4** (25.0 mg, 43%) as a red solid. ^{1}H-NMR (400 MHz, CD_3OD): δ 8.19 (d, 2H, *J* = 8.5 Hz), 7.95 (d, 4H, *J* = 9.0 Hz), 7.88 (d, 2H, *J* = 13.5 Hz), 7.66–7.57 (m, 4H), 7.50–7.40 (m, 7H), 6.15 (d, 2H, *J* = 13.5 Hz), 4.33 (t, 4H, *J* = 7.6 Hz), 3.92 (s, 2H), 3.83–3.78 (m, 4H), 2.98 (t, 4H, *J* = 7.0 Hz), 2.90–2.85 (m, 4H), 2.59 (t, 4H, *J* = 6.5 Hz), 2.31–2.21 (m, 4H), 1.92 (s, 12H), 1.88–1.81 (m, 2H). HRMS (ESI$^-$): calcd. for $C_{55}H_{61}N_4O_6S_2$ [M−Na]$^-$ 937.4038, found: 937.4057 (+1.9 mmu).

Preparation of 5: Compound **1** (52.8 mg, 64.3 μmol), *N*,*N*,*N'*-trimethylethylenediamine (23.4 μL, 180 μmol), and NEt_3 (40.0 μL, 287 μmol) were dissolved in anhydrous DMF (4 mL). Then, the mixture was reacted and purified according to the general procedure to afford **5** (25.4 mg, 45%) as a purple solid. ^{1}H-NMR (400 MHz, CD_3OD): δ 8.17 (d, 2H, *J* = 8.5 Hz), 7.96–7.91 (m, 4H), 7.86 (d, 2H, *J* = 13.5 Hz), 7.59–7.53 (m, 4H), 7.39 (t, 2H, *J* = 7.6 Hz), 6.12 (d, 2H, *J* = 13.5 Hz), 4.32 (t, 4H, *J* = 7.0 Hz), 3.95 (t, 2H, *J* = 5.4 Hz), 3.51 (s, 3H), 2.99 (t, 4H, *J* = 7.2 Hz), 2.81–2.76 (m, 2H), 2.60 (t, 4H, *J* = 10.0 Hz) , 2.33–2.22 (m, 10H), 1.97 (s, 12H), 1.90–1.84 (m, 2H). HRMS (ESI$^-$): calcd. for $C_{49}H_{59}N_4O_6S_2$ [M−Na]$^-$ 863.3882, found: 863.3893 (+1.1 mmu).

Preparation of 6: Compound **1** (50.0 mg, 60.9 μmol), 1,3-propanediamine (30.0 μL, 356 μmol), and NEt_3 (40.0 μL, 287 μmol) were dissolved in anhydrous DMF (5 mL). Then, the mixture was reacted and purified according to the general procedure to afford **6** (16.3 mg, 31%) as a blue solid. ^{1}H-NMR (400 MHz, CD_3OD): δ 8.15 (d, 2H, *J* = 9.9 Hz), 7.93–7.86 (m, 6H), 7.55–7.49 (m, 4H,), 7.35 (t, 2H, *J* = 7.6 Hz), 6.00–5.92 (m, 2H), 4.31–4.24 (m, 4H), 3.91 (t, 2H, *J* = 6.5 Hz), 2.98 (t, 4H, *J* = 8.1 Hz), 2.90 (t, 2H, *J* = 6.5 Hz), 2.63 (t, 4H, *J* = 6.3 Hz), 2.30–

2.23 (m, 4H), 2.03–1.91 (m, 14H), 1.89–1.83 (m, 2H). HRMS (ESI$^+$): calcd. for $C_{47}H_{56}N_4NaO_6S_2$ $[M+Na]^+$ 859.3534, found: 859.3543 (+0.9 mmu).

Preparation of 7: Compound **1** (51.6 mg, 61.2 μmol), *N*,*N*,*N'*-trimethyl-1,3-propanediamine (26.4 μL, 180 μmol), and NEt_3 (40.0 μL, 287 μmol) were dissolved in anhydrous DMF (4 mL). Then, the mixture was reacted and purified according to the general procedure to afford **7** (28.2 mg, 51%) as a purple solid. ^{1}H-NMR (400 MHz, CD_3OD): δ 8.19 (d, 2H, *J* = 8.5 Hz), 7.98–7.91 (m, 4H), 7.78 (d, 2H, *J* = 13.0 Hz), 7.63–7.54 (m, 4H), 7.40 (t, 2H, *J* = 7.6 Hz), 6.16 (d, 2H, *J* = 13.0 Hz), 4.34 (t, 4H, *J* = 6.7 Hz), 3.84 (t, 2H, *J* = 6.3 Hz), 3.50 (s, 3H), 2.99 (t, 4H, *J* = 7.0 Hz), 2.62 (t, 4H, *J* = 7.6 Hz), 2.39 (t, 2H, *J* = 7.4 Hz), 2.33–2.23 (m, 10H) , 2.09–1.96 (m, 14H), 1.91–1.84 (m, 2H). HRMS (ESI$^-$): calcd. for $C_{50}H_{61}N_4O_6S_2$ $[M-Na]^-$ 877.4049, found: 877.4038 (−1.1 mmu).

Preparation of 8: Compound **1** (50.0 mg, 60.9 μmol), methylamine (10.3 μL, 232 μmol), and NEt_3 (60.0 μL, 431 μmol) were dissolved in anhydrous DMF (2 mL). Then, the mixture was reacted and purified according to the general procedure to afford **8** (29.3 mg, 59%) as a red solid. ^{1}H-NMR (400 MHz, CD_3OD): δ 8.13 (d, 2H, *J* = 8.5 Hz), 7.89 (d, 4H, *J* = 8.5 Hz), 7.79 (d, 2H, *J* = 13.5 Hz), 7.55–7.45 (m, 4H), 7.34 (t, 2H, *J* = 7.2 Hz), 5.92 (d, 2H, *J* = 13.5 Hz), 4.29–4.20 (m, 4H), 3.51 (s, 3H), 3.02–2.93 (m, 4H), 2.69–2.61 (m, 4H), 2.31–2.21 (m, 4H), 2.03–1.82 (m, 14H). HRMS (ESI$^-$): calcd. for $C_{45}H_{50}N_3O_6S_2$ $[M-Na]^-$ 792.3147, found: 792.3171 (+2.4 mmu).

Preparation of 9: Compound **1** (53.8 mg, 65.5 μmol), dimethylamine (20.0 μL, 297 μmol), and NEt_3 (60.0 μL, 431 μmol) were dissolved in anhydrous DMF (3 mL). Then, the mixture was reacted and purified according to the general procedure to afford **9** (32.4 mg, 60%). ^{1}H-NMR (400 MHz, CD_3OD): δ 8.16 (d, 2H, *J* = 8.1 Hz), 7.91 (d, 4H, *J* = 7.6 Hz), 7.65 (d, 2H, *J* = 13.0 Hz), 7.57–7.50 (m, 4H), 7.37 (t, 2H, *J* = 7.4 Hz), 6.04 (d, 2H, *J* = 13.0 Hz), 4.32–4.24 (m, 4H), 3.59 (s, 6H), 2.98 (t, 4H, *J* = 7.0 Hz), 2.60 (t, 4H, *J* = 5.6 Hz), 2.31–2.21 (m, 4H), 1.99–1.82 (m, 14H). HRMS (ESI$^-$): calcd. for $C_{46}H_{52}N_3O_6S_2$ $[M-Na]^-$ 806.3303, found: 806.3315 (+1.2 mmu).

Preparation of 10: Compound **1** (62.0 mg, 60.9 μmol), piperidine (18.7 μL, 189 μmol), and NEt_3 (60.0 μL, 431 μmol) were dissolved in anhydrous DMF (7 mL). Then, the mixture was reacted and purified according to the general procedure to afford **10** (22.2 mg, 42%) as a purplish red solid. ^{1}H-NMR (400 MHz, CD_3OD): δ 8.18 (d, 2H, *J* = 8.1 Hz), 7.95–7.89 (m, 4H), 7.81 (d, 2H, *J* = 13.5 Hz), 7.59–7.52 (m, 4H), 7.38 (t, 2H, *J* = 7.4 Hz), 6.09 (d, 2H, *J* = 13.5 Hz), 4.34–4.26 (m, 4H) , 3.92–3.83 (m, 4H), 2.98 (t, 4H, *J* = 7.0 Hz), 2.61 (t, 4H, *J* = 6.7 Hz), 2.31–2.21 (m, 4H), 2.03–1.94 (m, 18H), 1.91–1.83 (m, 2H). HRMS (ESI$^-$): calcd. for $C_{49}H_{56}N_3O_6S_2$ $[M-Na]^-$ 846.3616, found: 846.3640 (+2.4 mmu).

Preparation of 11: Compound **1** (50.0 mg, 60.9 μmol), β-alanine (16.0 mg, 180 μmol), and NEt_3 (40.0 μL, 287 μmol) were dissolved in anhydrous DMF (7 mL). Then, the mixture was reacted and purified according to the general procedure to afford **11** (8.50 mg, 16%) as a purple solid. ^{1}H-NMR (400 MHz, CD_3OD): δ 8.21 (d, 2H, *J* = 8.5 Hz), 7.95–7.87 (m, 6H), 7.56–7.49 (m, 4H), 7.35 (t, 2H, *J* = 7.2 Hz), 5.99 (d, 2H, *J* = 13.0 Hz), 4.26 (t, 4H, *J* = 7.6 Hz), 3.98 (t, 2H, *J* = 5.4 Hz), 2.98 (t, 4H, *J* = 7.0 Hz), 2.65–2.57 (m, 6H), 2.30–2.22 (m, 4H), 1.99 (s, 12H), 1.91–1.84 (m, 2H). HRMS (ESI^-): calcd. for $C_{47}H_{51}N_3O_8S_2$ $[M-H-Na]^{2-}$ 424.6564, found: 424.6569 (+0.5 mmu).

Preparation of 12: Compound **1** (50.0 mg, 60.9 μmol), 6-aminohexanoic acid (23.8 mg, 181 μmol), and NEt_3 (40.0 μL, 287.0 μmol) were dissolved in anhydrous DMF (5 mL). Then, the mixture was reacted and purified according to the general procedure to afford **12** (19.5 mg, 35%) as a dark red solid. ^{1}H-NMR (400 MHz, CD_3OD): δ 8.17 (d, 2H, *J* = 8.5 Hz), 7.93–7.84 (m, 6H), 7.58–7.50 (m, 4H), 7.35 (t, 2H, *J* = 7.6 Hz), 5.99 (d, 2H, *J* = 13.0 Hz), 4.26 (t, 4H, *J* = 10.0 Hz), 3.82 (t, 2H, *J* = 6.7 Hz), 2.98 (t, 4H, *J* = 7.0 Hz), 2.62 (t, 4H, *J* = 6.3 Hz), 2.30–2.20 (m, 6H), 1.97 (s, 12H), 1.91–1.84 (m, 4H), 1.77–1.70 (m, 2H), 1.56–1.49 (m, 2H). HRMS (ESI^-): calcd. for $C_{50}H_{58}N_3O_8S_2$ $[M-Na]^-$ 892.3671, found: 892.3688 (+1.7 mmu).

Preparation of 13: Compound **1** (62.3 mg, 71.1 μmol) and morpholine (60.0 mg, 689 μmol) were dissolved in anhydrous DMF. Then, the mixture was reacted and purified according to the general procedure to afford **13** (18.4 mg, 30%) as a red solid. ^{1}H-NMR (400 MHz, CD_3OD): δ 8.22 (d, 2H, *J* = 8.5 Hz), 8.02–7.91 (m, 6H), 7.64–7.55 (m, 4H), 7.41 (t, 2H, *J* = 7.6 Hz), 6.20 (d, 2H, *J* = 13.5 Hz), 4.36 (t, 4H, *J* = 7.6 Hz), 4.07–4.01 (m, 4H) , 3.81–3.76 (m, 4H) , 2.99 (t, 4H, *J* = 7.0 Hz) , 2.63 (t, 4H, *J* = 6.5 Hz), 2.33–2.23 (m, 4H), 2.02 (s, 12H), 1.91–1.84 (m, 2H). HRMS (ESI^-): calcd. for $C_{48}H_{54}N_3O_7S_2$ $[M-Na]^-$ 848.3409, found: 848.3418 (+0.9 mmu).

Preparation of 14: Compound **1** (50.0 mg, 60.9 μmol), 1-acetylpiperazine (21.5 μL, 180 μmol), and NEt_3 (40.0 μL, 287 μmol) were dissolved in anhydrous DMF (5 mL). Then, the mixture was reacted and purified according to the general procedure to afford **14** (17.3 mg, 31%) as a purplish red solid. ^{1}H-NMR (400 MHz, CD_3OD): δ 8.22 (d, 2H, *J* = 8.5 Hz), 8.02 (d, 2H, *J* = 13.5 Hz), 7.99–7.92 (m, 4H), 7.64–7.56 (m, 4H), 7.42 (t, 2H, *J* = 7.6 Hz), 6.25 (d, 2H, *J* = 13.5 Hz), 4.39 (t, 4H, *J* = 7.9 Hz), 3.98–3.88 (m, 4H), 3.74–3.65 (m, 4H), 2.99 (t, 4H, *J* = 7.0 Hz), 2.65 (t, 4H, *J* = 6.5 Hz), 2.33–2.24 (m, 7H), 2.01 (s, 12H), 1.92–1.85 (m, 2H). HRMS (ESI^-): calcd. for $C_{50}H_{57}N_4O_7S_2$ $[M-Na]^-$ 889.3674, found: 889.3706 (+3.2 mmu).

Preparation of 15: Compound **1** (50.0 mg, 60.9 μmol), 1-(methanesulfonyl)piperazine (29.6 mg, 200 μmol), and NEt_3 (40.0 μL, 287 μmol) were dissolved in anhydrous DMF (5 mL). Then, the mixture was reacted and purified according to the general procedure to afford **15** (11.6 mg, 20%) as a blue solid. ^{1}H-NMR (400 MHz,

CD_3OD): δ 8.24 (d, 2H, *J* = 8.5 Hz), 8.08 (d, 2H, *J* = 13.0 Hz), 8.00–7.93 (m, 4H), 7.65 (d, 2H, 8.5 Hz), 7.60 (t, 2H, *J* = 7.8 Hz), 7.43 (t, 2H, *J* = 7.8 Hz), 6.29 (d, 2H, *J* = 13.5 Hz), 4.41 (t, 4H, *J* = 7.4 Hz), 3.76–3.70 (m, 4H), 3.61–3.56 (m, 4H), 3.12 (s, 3H), 2.99 (t, 4H, *J* = 7.0 Hz), 2.66 (t, 4H, *J* = 6.3 Hz), 2.34–2.24 (m, 4H), 2.04 (s, 12H), 1.92–1.85 (m, 2H). HRMS (ESI^-): calcd. for $C_{49}H_{57}N_4O_8S_3$ $[M-Na]^-$ 925.3344, found: 925.3366 (+2.2 mmu).

Preparation of 16: Compound **1** (50.0 mg, 60.9 μmol), **S6** (43.6 mg, 180 μmol, see supporting information for synthesis of **S6**), and NEt_3 (40.0 μL, 287 μmol) were dissolved in anhydrous DMF (5 mL). The mixture was stirred at 80 ºC for 1.5 h under an argon atmosphere. Then, further NEt_3 (1.00 mL, 7.20 mmol) was added to the mixture. The mixture was reacted and purified according to the general procedure to afford **16** (8.40 mg, 16%) as a gray solid. Since **16** underwent decomposition during the NMR measurements, it was analyzed by LC-MS and its purity was confirmed by HPLC (**Figure S1**). HRMS (ESI^+): calcd. for $C_{50}H_{60}N_4NaO_6S_2$ $[M+Na]^+$ 899.3847, found: 899.3875 (+0.1 mmu).

Preparation of 17: Compound **1** (50.0 mg, 60.9 μmol), 3-(piperazin-1-yl)propanoic acid (28.9 mg, 182 μmol), and NEt_3 (50.7 μL, 364 μmol) were dissolved in anhydrous DMF (4 mL). Then, the mixture was reacted and purified according to the general procedure to afford **17** (10.5 mg, 18%) as a purplish red solid. ^{1}H-NMR (400 MHz, CD_3OD): δ 8.22 (d, 2H, *J* = 8.5 Hz), 7.97–7.89 (m, 6H), 7.62–7.56 (m, 4H), 7.40 (t, 2H, *J* = 7.0 Hz), 6.16 (d, 2H, *J* = 13.5 Hz), 4.34 (t, 4H, *J* = 7.6 Hz), 3.84 (t, 4H, *J* = 3.8 Hz), 3.02–2.88 (m, 10H), 2.62 (t, 4H, *J* = 6.5 Hz), 2.54 (t, 4H, *J* = 7.6 Hz), 2.32–2.23 (m, 4H), 2.02 (s, 12H), 1.90–1.84 (m, 2H). HRMS (ESI+): calcd. for $C_{51}H_{58}N_4Na_3O_8S_2$ $[M+Na]^+$ 987.3384, found: 987.3367 (−1.7 mmu).

Preparation of 18: Compound **1** (54.2 mg, 66.0 μmol), **S7** (49.2 mg, 210 μmol), and NEt_3 (50.0 μL, 359 μmol) were dissolved in anhydrous DMF (3 mL). Then, the mixture was reacted and purified according to the general procedure to afford **18** (12.5 mg, 19%) as a red solid. ^{1}H-NMR (400 MHz, CD_3OD): δ 8.21 (d, 2H, *J* = 9.0 Hz), 7.97–7.92 (m, 4H), 7.88 (d, 2H, *J* = 13.5 Hz), 7.64 (t, 2H, *J* = 7.2 Hz), 7.59 (d, 2H, *J* = 9.0 Hz), 7.44–7.38 (m, 6H), 6.15 (d, 2H, *J* = 13.5 Hz), 4.33 (t, 4H, *J* = 7.6 Hz), 3.86–3.80 (m, 6H), 3.50 (s, 2H), 2.99 (t, 4H, *J* = 7.0 Hz), 2.90–2.83 (m, 4H), 2.60 (t, 4H, *J* = 6.5 Hz), 2.31–2.22 (m, 4H), 1.97 (s, 12H), 1.90–1.82 (m, 2H). HRMS (ESI^-): calcd. for $C_{57}H_{63}N_4O_8S_2$ $[M-Na]^-$ 995.4093, found: 995.4109 (+1.6 mmu).

Preparation of 19: Compound **1** (50.0 mg, 60.9 μmol), 2-(piperidin-4-yl)acetic acid (25.8 mg, 180 μmol), and NEt_3 (60.0 μL, 431 μmol) were dissolved in anhydrous DMF (7 mL). Then, the mixture was reacted and purified according to the general procedure to afford **19** (28.4 mg, 50%). ^{1}H-NMR (400 MHz, CD_3OD): δ 8.22 (d, 2H, *J* = 8.5 Hz), 7.95–7.89 (m, 4H), 7.84 (d, 2H, *J* = 13.5 Hz), 7.60–7.54 (m, 4H), 7.38 (t, 2H, *J* = 7.4 Hz), 6.11

(d, 2H, *J* = 13.0 Hz), 4.31 (t, 4H, *J* = 7.4 Hz), 4.07–3.99 (m, 2H), 3.71 (t, 2H, *J* = 10.0 Hz), 2.99 (t, 4H, *J* = 7.0 Hz), 2.61 (t, 4H, *J* = 6.5 Hz), 2.38–2.21 (m, 6H), 2.14–2.07 (m, 2H), 2.00 (s, 12H), 1.91–1.82 (m, 2H), 1.73–1.60 (m, 2H). HRMS (ESI$^-$): calcd. for $C_{51}H_{58}N_3O_8S_2$ $[M-Na]^-$ 904.3671, found: 904.3681 (+1.0 mmu).

General procedure for the preparation of cyanine dye-antibody conjugates: Each cyanine dye (1 eq), *N*,*N*,*N'*,*N'*-tetramethyl-*O*-(*N*-succinimidyl)uronium tetrafluoroborate (TSTU) (2.0–2.1 eq), and NEt_3 (3.0–4.5 eq) were dissolved in anhydrous DMF (1.0–1.4 mL/μmol). The mixture was stirred at room temperature for 1 h. The reaction progress was monitored by HPLC (A/B = 0.1 M triethylamine acetate (TEAA) buffer/99% MeCN, 1% H_2O). Subsequently, TFA was added to the mixture to neutralize the pH. Then, DMF was removed under vacuum and the precipitate was dried under vacuum. The crude product was used in the next step without further purification. The crude product was dissolved in DMSO (30 μL) to prepare a 5.8–10.5 mM DMSO solution. The DMSO solution (purity: 67%, 2.63 μL, 10.15 nmol) and 32.7 mg/mL panitumumab in PBS (9.17 μL, 2.03 nmol) were added to 0.1 M Na_2HPO_4 aq. containing 5% DMSO toa total volume of 300 μL. The mixture was left at room temperature for 3 h. Upon reaction completion, the mixture was purified by using an Amicon Ultra-4 30 kDa (Merck KGaA) filter. The protein concentration of the product was measured with a microplate reader (infinite M200, TECAN) using a BCA protein assay kit (Thermo Fisher Scientific K.K.) and dye concentration was calculated by absorbance measurements using a UV-Vis spectrophotometer (UV-1800, Shimazu Co.). The ratios of antibody to dye were found to be 1:3–8, which included dyes binding to antibodies or dyes connected via non-covalent binding due to their hydrophobicity.

Preparation of C1: Dye **17** (1.93 mg, 2 μmol), TSTU (1.20 mg, 3.99 μmol), and NEt_3 (1.00 μL, 8.90 μmol) were dissolved in anhydrous DMF (2 mL). The mixture was then reacted and purified according to the general procedure. The conjugation reaction was performed using a 5.8 mM DMSO solution (purity: 67%, 2.63 μL, 10.15 nmol). The ratio of antibody to dye in **C1** was found to be 1:3.

Preparation of C2: Dye **18** (2.04 mg, 2.00 μmol), TSTU (1.20 mg, 3.99 μmol), and NEt_3 (1.00 μL, 8.90 μmol) were dissolved in anhydrous DMF (2 mL). The mixture was then reacted and purified according to the general procedure. The conjugation reaction was performed using a 10.5 mM DMSO solution (purity: 36%, 2.67 μL, 10.09 nmol). The ratio of antibody to dye in **C2** was found to be 1:8.

Preparation of C3: Dye **19** (1.78 mg, 2.15 μmol), TSTU (1.36 mg, 4.52 μmol), and NEt_3 (0.89 μL, 6.39 μmol) were dissolved in anhydrous DMF (3 mL). The mixture was then reacted and purified according to the general procedure. The conjugation reaction was performed using a 6.4 mM DMSO solution (purity: 60%, 2.64 μL,

10.2 nmol). The ratio of antibody to dye in **C3** was found to be 1:5.

2.2. PA measurements in aqueous solutions

PA signals in aqueous solutions were detected using a home-build set up, as shown in **Figure S2** [16]. An excitation pulse light (6–8 nsec) was generated using a wavelength-tunable OPO laser system (Versascan MBI-FE, Spectra Physics or PrimoScan BMU-SE, Spectra Physics) excited by a Nd:YAG laser (Quanta-Ray Pro-190-THDA-FE, Spectra Physics) with a repetition frequency of 10 Hz. The excitation pulse light was shaped to have a 3 mm diameter beam, focused using an 18.24 mm focal length lens, and introduced into a multimode optical fiber (M40L02, Thorlabs, Newton, NJ, USA) with a core diameter of 400 μm and an NA of 0.48. To correct potential output energy fluctuations, the pulse light was split using a beam sampler, and the energy of the split light was measured using an energy meter (PE10-C, Ophir Optics, Jerusalem, Israel). The output end of the multimode optical fiber was fixed at the center of an ultrasonic sensor with a ring-shaped detection element (inner diameter 1.4 mm, outer diameter 3.0 mm). The detection surface of the ultrasonic sensor was submerged in a small water tank filled with degassed water. The bottom surface of the small water tank was made of a glass cover that transmitted both light and ultrasonic waves, and the distance between the detection surface of the ultrasonic sensor and the glass cover was set to 10 mm. The excitation pulse light from the multimode optical fiber was irradiated into the liquid column, and the resulting ultrasound was observed using the ultrasonic sensor. The signal was then amplified using an FET amplifier (SA220F5, NF Circuit Design Block, Kanagawa) and recorded using a digital oscilloscope (M9210A, Agilent technology, Santa Clara, CA).

Dyes were dissolved in a 50% 0.01 M phosphate buffer/50% DMSO solution at pH 3.5 or 7.0 and at a final concentration of 10 μM. The solution was then dropped onto a glass slide, and the glass cover on the bottom surface of the small water tank was brought into contact with the liquid surface of the solution, adjusting the gap between the glass cover and the glass slide to 1 mm. Then, PA measurements were performed at 5 nm intervals in the 500−1000 nm range for **5**, **7**, and **8** and at 10 nm intervals in the 500−1000 nm range for **17**–**19**. To investigate sample changes due to photobleaching or aggregation, measurements were performed at 10 nm intervals in the 500–1000 nm range, followed by 10 nm intervals in the 505–995 nm range for **5**, **7**, and **8**, and at 20 nm intervals in the 500–1000 nm range, followed by 20 nm intervals in the 505–995 nm range for **17**–**19**. At each excitation wavelength, 50 photoacoustic signal measurements were conducted, and the intensity peak values of the averaged signals were measured. These values were then normalized by the energy of the irradiated excitation pulse light to determine the photoacoustic signal intensity at each excitation wavelength.

2.3. Fluorescence imaging with cyanine dye-antibody conjugates in cultured cancer cells

Fluorescence imaging in cultured cells was performed using a BX41 upright fluorescence microscope (Olympus) equipped with a UPlanSApo 40x objective lens (Olympus). Images were captured with an Exi Aqua monochrome camera (Q imaging) and an acquisition software (Q Capture Pro, Q imaging). The microscope used a U-DM-Cy7-3 filter (Olympus, Excitation: 673–748 nm, Emission: 765–855 nm) and U-RFL-T excitation light source (Olympus).

HuCCT-1 cells were seeded in a 35 mm dish containing a glass cover and incubated at 37 °C with 5% CO_2. After one day, antibody-dye conjugates were added to the dish at a final concentration of 5 μg/mL and incubated for 24 h. The glass cover was removed from the dish, washed with phenol red-free medium, and placed on a slide with the cell side facing down. Subsequently, the slide was set up in a fluorescence microscope, and the fluorescence was determined. Image processing and analysis were performed using an Image J software version 1.52.

2.4. PA imaging with cyanine dye-antibody conjugates in cultured cancer cells

PA imaging in cultured cells was performed using a home-build set up, as shown in **Figure S3**. A wavelength-tunable nanosecond pulsed laser (NT342A-10-AW, EKSPLA, pulse duration, 5 nsec; repetition rate, 10 Hz) was employed as the laser source. The excitation pulse light was collimated to form a 1 cm diameter beam and then adjusted for pulse energy using a wave plate (1/2λ plate), polarizing plate, and ND filter. The light was focused onto the dish using a LUMPLFLM 40x water-immersion objective lens (Olympus). The photoacoustic waves from the sample were detected by an acoustic transducer (10K6.4I PF15, Japan Probe, focal length, 15 mm; center frequency, 10 MHz) in the water bath. The photoacoustic signal was amplified through a low-pass filter (BLP-21.4+, Mini-Circuits, bandwidth; DC-22MHz) and an amplifier (AU-1647, MITEQ, bandwidth; 0.1 K–400 MHz, gain; 57 dB), and then recorded using a digital oscilloscope (DS-5654A, IWATSU). To correct for potential variations in output energy, pulse light energy was measured by placing a pyroelectric energy sensor (919E-0.1-12-25K, Newport) at the position where the dish was placed. The acquired photoacoustic signal was normalized by the measured excitation light pulse energy. A laser diode was positioned where the reflected light from the ND filter passes, and the photoacoustic signal was measured only when the pulse light intensity was sufficient. Photoacoustic images were generated as two-dimensional images by scanning the sample in a zigzag pattern using a stepping motor stage (TAMM100-50C and HSC-103, OptoSigma) and projecting the peak envelope intensity values of each acquired photoacoustic signals. Bright field images were observed using a CMOS camera (DCC1645C, Thorlabs).

HuCCT-1 cells were seeded in 35 mm dishes and incubated at 37°C with 5% CO_2. After one day,

antibody-dye conjugates were added to the dish at a final concentration of 5 μg/mL and incubated for 24 h. Subsequently, the bottom surface of the cell dish was put in contact with a water bath set to 37 °C, and PA imaging was performed at 675 and 800 nm. Image processing and analysis were performed using an Image J software version 1.52.

3. RESULTS

3.1. Design and synthesis of cyanine dyes bearing amino groups

To develop pH-responsive PA imaging agents, we designed Cy7.5 derivatives having either a piperazin-1-yl group or various amino groups as pH-sensing moieties at the central carbon of the polymethine chain (**Figure 1**). These Cy7.5 derivatives feature a cyclohexene ring in their structure for ease of synthesis and two sulfonate groups for improving water solubility. Various substituents were installed at the pH-sensing moiety, such as carboxy, alkyl, amide, sulfonamide, and additional amino groups, to compare their influence on pH-responsiveness. All Cy7.5 derivatives were synthesized as illustrated in **Scheme 1**. Cyanine dye intermediate **1**, which carries a chloro group at the center of the polymethine chain, was firstly synthesized over three steps according to a previous report (**Scheme S1**) [17,18]. Then, piperazine and its analogues were introduced in the cyanine structure via nucleophilic substitution in DMF to afford a set of dyes with different pH-sensing moieties (**2**–**16**; **Scheme 1**). All compounds were characterized by NMR and HRMS analyses.

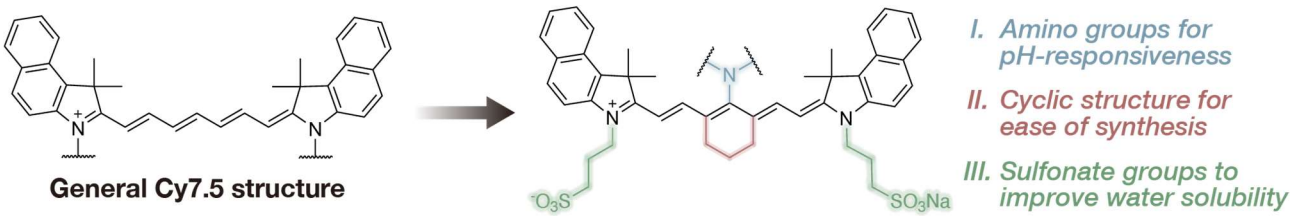

Figure 1. Design of cyanine dyes bearing amino groups.

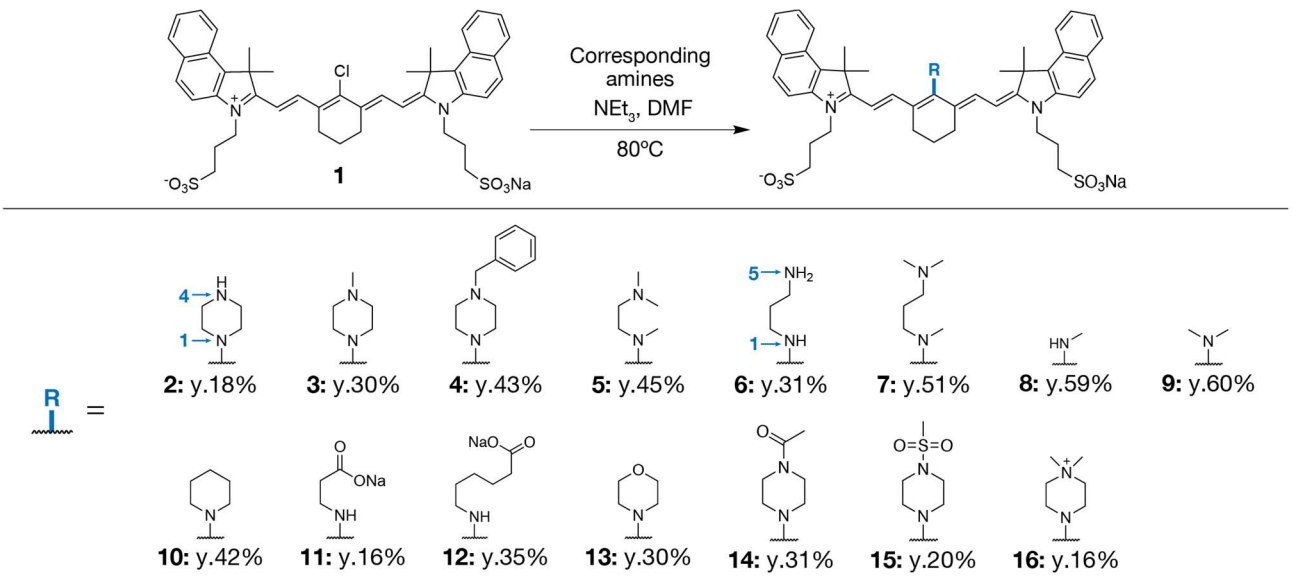

Scheme 1. Synthetic procedure and chemical structures of dyes bearing amino groups.

3.2. Investigation of the pH responsiveness of amine-substituted cyanine dyes using absorption spectroscopy

To examine the pH responsiveness of the dyes, their absorption spectra were measured in a phosphate buffer containing 30% DMSO at pH 3–12 (**Figure 2**). Dye **16** exhibited a small absorbance value in both phosphate buffer and DMSO (**Figures 2o**, **S1o**). This was probably due to the nucleophilic attack of some species such as hydroxide anions on the electron deficient cyanine structure, inducing decomposition. As shown in **Figure 2a**–**f**, the absorption spectra of all the dyes containing a diazaalkyl group (**2**–**7**) changed depending on the pH, and the absorption peaks around 800 nm increased at acidic pH, which is similar to the spectral changes of Cy7 dyes reported by Nagano's group [12]. In particular, the spectral changes of the dyes with a 1,4-diazaalkyl group (**2**–**5**) were larger than those observed for the dyes with a 1,5-diazaalkyl group (**6**–**7**). In contrast, the absorption spectra of the dyes with a monoamine (**8**–**10**), carboxylate (**11**–**12**), morpholin-4-yl (**13**), amide (**14**–**15**), and quaternary ammonium salt (**16**) moiety did not change with pH variations (**Figure 2g**–**o**). These results suggested that pH-dependent spectral changes were induced by the amino groups at position 4 or 5 in the pH-sensing moiety. Similar investigations were also performed in a DMSO solution. It is known that cyanine dyes can easily form J-aggregates in aqueous solutions and less likely in organic solvents [19–21]. However, cyanine dyes **2–16** exhibited a similar spectral behavior in DMSO as well as in mixtures of DMSO and phosphate buffer, as shown in **Figure S4**. These findings indicated that the observed spectral changes were probably not affected by aggregation but rather protonation of the pH-sensing moiety.

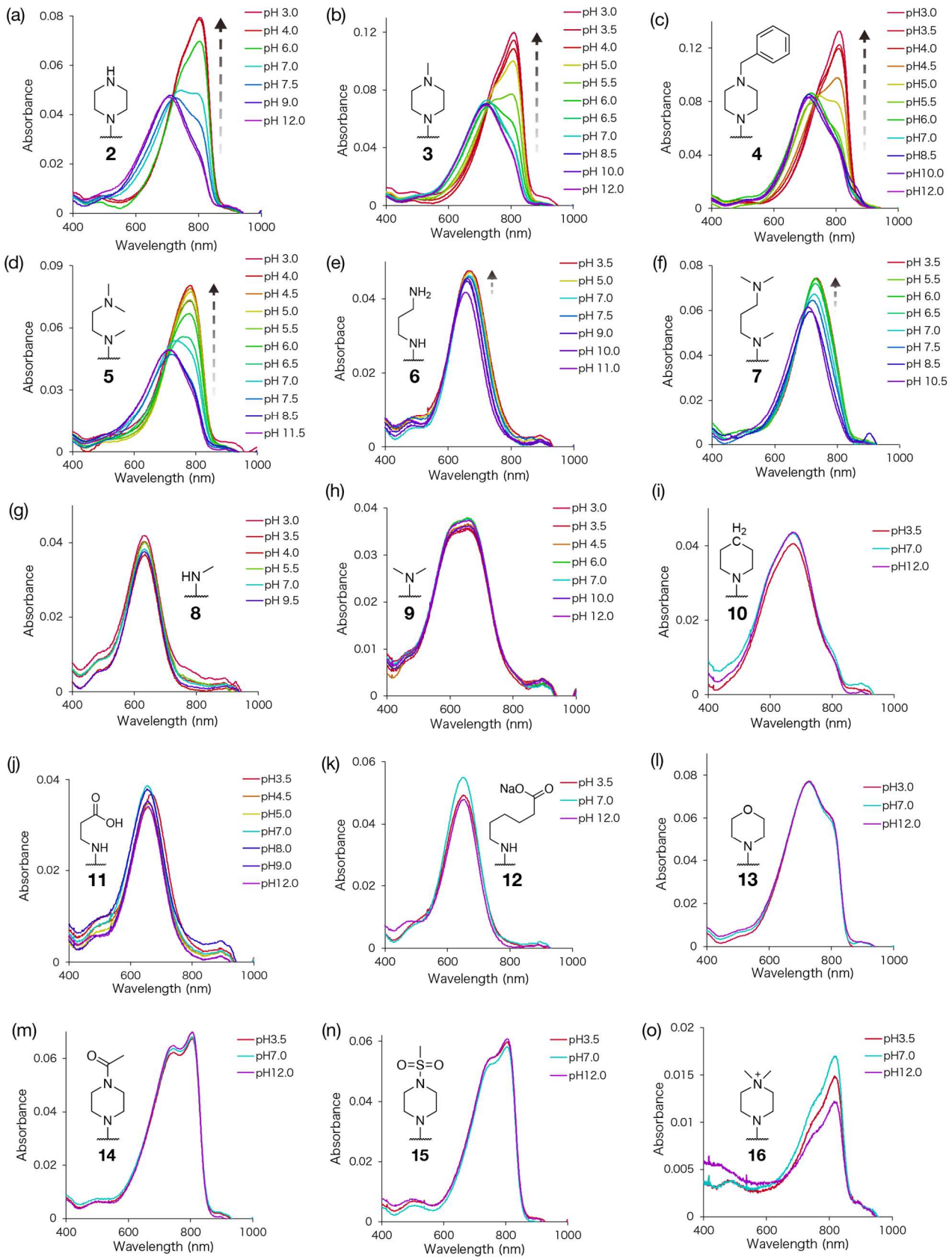

Figure 2. Absorption spectra of the dyes bearing various amino groups. Absorption spectra of (a) **2**, (b) **3**, (c) **4**, (d) **5**, (e) **6**, (f) **7**, (g) **8**, (h) **9**, (i) **10**, (j) **11**, (k) **12**, (l) **13**, (m) **14**, (n) **15**, and (o) **16** were measured in phosphate buffer containing 30% DMSO at pH 3.0–12.0. The final concentration of each dye was 1 μM.

3.3. Optical and chemical properties of dyes bearing amino groups

To investigate the optical properties of amino group substituted **2**–**16**, the fluorescence spectra were measured in PB with 30% DMSO or DMSO (**Figures S5**–**S6**). From the absorption and fluorescence spectra obtained, the optical properties of **2**–**16** [i.e., absorption maximum wavelength (Abs_{max}), fluorescence maximum wavelength (Em_{max}), Stokes shift (Δλ), molar extinction coefficient (ε), fluorescence quantum yield (φ_f), and p*K*a] were determined and are summarized in **Table 1**. The p*K*a of the dyes with a 1,4- or 1,5-diazaalkyl group (**2**–**7**) were found to be in the range of 4.7–7.3 (**Figure S7**). Dye **4** bearing a benzyl group showed a lower p*K*a than methyl-substituted dye **3**, indicating that the presence of an electron withdrawing benzyl group affected the protonating capacity of the pH-sensing moiety (**Figure S7b**–**c**). On the other hand, dye **2** showed a higher p*K*a than **3**, which may be due to the difference of hydration energy between the protonated forms of secondary and tertiary amines (**Figure S7a**–**b**). Generally, hydration and consequential stabilization of protonated tertiary amines is more difficult than that of secondary amines due to their higher bulkiness. Therefore, secondary amines exhibit higher p*K*a values than tertiary amines (e.g., p*K*a of dimethylamine: 10.73, p*K*a of trimethylamine: 9.75) [22].

The reversibility of the absorption spectra variation was also investigated by changing the pH using trifluoroacetic acid (TFA) as organic acid and triethylamine (NEt_3) as organic base (**Figure S8**). When an excess of TFA was added to a solution of either **5** (a dye with a 1,4-diazaalkyl group) or **7** (a dye with a 1,5-diazaalkyl group) in DMSO, red-shifts were observed. Furthermore, when adding an excess of NEt_3 to the red-shifted solutions, blue-shifts were observed. These results indicated that the spectral properties of the dyes could undergo reversible changes in response to pH.

Table 1. Optical properties of dyes bearing amino groups at acidic pH and basic pH.

Compound	Abs_{max} (nm)[a]	Em_{max} (nm)[a]	Δλ (nm)[a]	ε ($M^{-1}cm^{-1}$)[a]	φ_f[b]	p*K*a[a]
2	706	832	126	4.7×10^4	0.09	-
2 ($+H^+$)	802	836	34	7.9×10^4	0.07	6.9
3	717	829	112	6.9×10^4	0.12	-
3 ($+H^+$)	810	838	28	1.2×10^5	0.07	5.5
4	707	829	122	8.3×10^4	0.08	-
4 ($+H^+$)	811	842	31	1.3×10^5	0.07	4.7
5	713	826	113	4.9×10^4	0.18	-
5 ($+H^+$)	780	830	50	8.0×10^4	0.13	6.6
6	658	800	142	4.2×10^4	0.16	-
6 ($+H^+$)	670	799	129	4.8×10^4	0.15	7.2
7	708	824	116	6.2×10^4	0.12	-
7 ($+H^+$)	733	825	92	7.4×10^4	0.10	7.3
8	632	805	173	3.8×10^4	0.22	-
9	659	818	159	3.7×10^4	0.13	-
10	674	823	149	4.3×10^4	0.11	-
11	653	800	147	3.9×10^4	0.32	-
12	651	799	148	5.5×10^4	0.18	-
13	728	831	103	7.7×10^4	0.09	-

14	804	832	28	6.8×10^4	0.09	-
15	805	834	29	5.8×10^4	0.10	-
16	815	846	31	1.7×10^4	0.07	-

a) phosphate buffer containing 30% DMSO, b) DMSO and DMSO with 1% TFA.

3.4. Effect of structural changes of the cyanine dyes at position 4 on the absorption spectra

Based on the observation that dyes with either a piperazin-1-yl (**2**–**4**) or 1,4-diazaalkyl (**5**) group at the pH-sensing moiety exhibited a significant acidity-dependent increase of absorbance around 800 nm (**Figure 2a**–**d**), it was assumed that protonation of the piperazine ring or 1,4-diazaalkyl structure was a key factor responsible for these spectral changes. Dyes with a 4-acetyl (**14**), 4-methanesulfonyl (**15**), and 4,4-dimethylpiperazinum-1-yl (**16**) group did not show significant spectral changes and a sharp absorbance peak around 800 nm was observed independent of pH (**Figure 3a**–**b**). In contrast, dyes with a 4-methylpiperazin-1-yl (**3**) in alkaline solution, piperidin-1-yl (**10**), and morpholin-4-yl (**13**) group, which do not have strong electron-withdrawing groups at position 4, exhibited smaller relative absorbances at 815 nm than **14** and **15**, and these absorption peaks blue-shifted. These results indicated that the sharp peak around 800 nm may increase when the 6-membered ring of the pH-sensing moiety is substituted with an electron-withdrawing group (**2**–**4** in their protonated form, and **14**–**16**). In other words, as the electron donating ability of the 6-membered ring increases (**2**–**4** in their unprotonated form, **10**, and **13**), the peak around 800 nm decreases, while that around 700 nm increases. The relative absorbance at 815 nm and the red-shift of the absorption peak for **3**, **10**, **13** were in the order of **13**>**3**>**10**, whose atoms of position 4 on their 6-membered amino group were O, N, and C, respectively. This implies that the electronegativity of the atom at position 4 also affects the absorption spectra of the dyes. Even in DMSO, where the influence of aggregates should be less than in water, absorption peaks around 800 nm increased when an electron-withdrawing group was introduced on the 6-membered ring (**Figure S9**). This finding also supported that the peak around 800 nm was not due to J-aggregation.

3.5. Elucidating the mechanism of spectral changes in the cyanine dyes using DFT analysis

It is known that polymethine dyes feature two types of structures: a cyanine form with delocalized charge across the conjugated system (low bond length alteration (BLA)) and a dipole form with localized charge (high BLA) (**Figure 4**) [14]. The transition between these structures is influenced by the presence of various substituents [23], solvent polarity [24], or counterions [25]. It was suggested that introducing electron-donating groups to the polymethine chain of the cyanine dyes results in enhancement of the contribution of the bis-dipole structure, making the absorption spectra blue-shifted [14]. Given that the bis-dipole structure forms a crossed-conjugated resonance configuration (**Figure 4**), dyes dominated by the bis-dipole structure will show the shorter C–N bond length and

larger bond order. Additionally, bis-dipole structure also results in localized charges in the conjugated system, with the central carbon atom becoming positively charged and the terminal N atoms negatively charged. To reveal the mechanism of the spectral changes of dyes with diazaalkyl groups, we estimated the length and bond order of the C–N bond connecting the nitrogen at position 1 to the central carbon in the polymethine chain (R(C–N)), BLA, and the natural charges on the nitrogen at position 1 of the 1-aza-6-membered ring (Charge(1-N)), the central carbon atom of the polymethine chain (Charge(C)), and the terminal nitrogen atom (Charge(terminal N)), using DFT calculations (LC-ωPBE/cc-pVDZ). These studies were conducted for dyes **3**, **10**, and **13**–**16**, as shown in **Figure 3**, **S10**, and **S11**. In model compounds, the two sulfopropyl groups introduced for water solubility purposes were replaced by methyl groups to simplify the calculations. **3'**, **10'**, **13'**–**16'** represent dyes in which the sulfopropyl side chains of **3**, **10**, **13**–**16** are replaced with methyl groups. **16'** possessed an overall smaller negative charge than the other dyes (**Figure S11**), most likely because the sp^3 ammonium cation made the structure electron deficient.

As shown in **Figure 3c**, the natural charge of the nitrogen atom at position 1 increased negatively in the order **10'**<**3'**<**13'**<**14'**<**16'**<**15'**, which corresponds to an order of increase of the electron density of the nitrogen atom (**Figure 3c**). Moreover, the C–N bond lengths decreased (C–N bond order decreased) in the following order **16'**>**15'**>**14'**>**13'**>**3'**>**10'**. These results indicated that the contribution of the cross-conjugation structure (resonance structure of bis-dipole form) decreased as the electron withdrawing ability of 6-membered amino groups increased. Focusing on the atom at position 4 of the pH-sensing moieties of dyes **3'**, **10'**, and **13'** (i.e., N, C, and O atom, respectively), it was seen that a dye carrying an atom of higher electronegativity possessed a more negatively charged N atom at position 1 and longer C–N bond length. When comparing Charge (C), Charge (terminal N), and BLA, which indicate charge localization within the bis-dipole structure, **14**–**16** bearing amides or ammonium exhibited lower values. These results suggest that the electron-withdrawing groups induce an increase in delocalized structures.

The calculation results were also compared with the normalized absorption peak intensities of the dyes at 815 nm (**Figure 3d**–**h**). As the natural charge increased negatively, the normalized absorbance at 815 nm increased (**Figure 3d**). On the other hand, as the C–N bond length increased, the normalized absorbance at 815 nm augmented, indicating the calculation results were correlated with the absorption peak intensities at 815 nm (**Figure 3e**). Further, when comparing the normalized absorbance at 815 nm with Charge (C), Charge (terminal N), and BLA of each dye, it was suggested that those with higher absorbance at 815 nm tend to have smaller positive Charge (C), negative Charge (terminal N), and small BLA values, suggesting more extensive charge delocalization (**Figure 3f–h**).

Considering the calculation results, dyes bearing weakly electron-withdrawing groups at position 4 (**3**, **10** and **13**), could have high contribution of the cross-conjugation form (the resonance structure of bis-dipole form) and charge-localized bis-dipole form, thus showing in blue-shifted absorption peak (~700 nm) (**Figure 4**). On the other hand, dyes bearing strong electron-withdrawing groups at position 4 (**14**–**16**) are thought to predominantly exhibit a delocalized structure, leading to an absorption peak around 800 nm. The results were similar to the absorption spectral changes of the cyanine dyes bearing various functional groups at position 1 reported by Maury's group [14]. Furthermore, dye **3** with an unprotonated N atom at position 4 and dye **16** with a positive charge on the N atom at position 4 exhibited absorption peaks around 700 and 800 nm, respectively. Accordingly, the pH-responsive mechanism of dyes with a 1,4-diazaalkyl group was assumed to be due to the changes in the contribution of bis-dipole form by protonation of the amino groups at position 4, which increased the electron-withdrawing ability of the pH-sensing moiety (**3** in **Figure 4**). From the investigation, we have concluded that electron-donating groups increase the contribution of the bis-dipole structure. However, given that these groups could lift the LUMO to enlarge the HOMO-LUMO gap (blue-shift), further investigation like TD-DFT calculations should be required.

Some studies reported that cyanine dyes with a piperazine derivative in the center of the polymethine chain stabilize one proton by means of the two amino groups of piperazine [12,26], as demonstrated for 1,8-bis(dimethylamino)naphthalene that is called "proton sponge" for trapping one proton by chelation by the two nitrogen atoms [27]. Our results, however, indicated that only one N atom at position 4 or 5 in the pH-sensing moiety was protonated since the absorption change was not dependent on the rigidity and distance between the two amino groups of the pH-sensing moiety (**Figure 2a**–**f**). If one proton would be trapped by two amino groups, an unusually high p*K*a should be found as in the case of a proton sponge (p*K*a 12.3) [28]. However, this was not observed for our piperazine based dyes (p*K*a 4.7–7.3) (**Figure S7**). The other paper previously reported that a pH-responsive fluorescent dye composed of piperazine and cyanine could undergo protonation at the amine neighboring the polymethine chain (position 1) inducing absorption spectral changes [22,28]. In the present study, dyes without a basic amino group in the pH-sensing moiety (**8**–**16**), however, did not show pH-dependent spectral changes at pH 3–12 (**Figure 2g**–**o**). Hence, the absorption spectral change cannot be due to the protonation of the amino group at position 1.

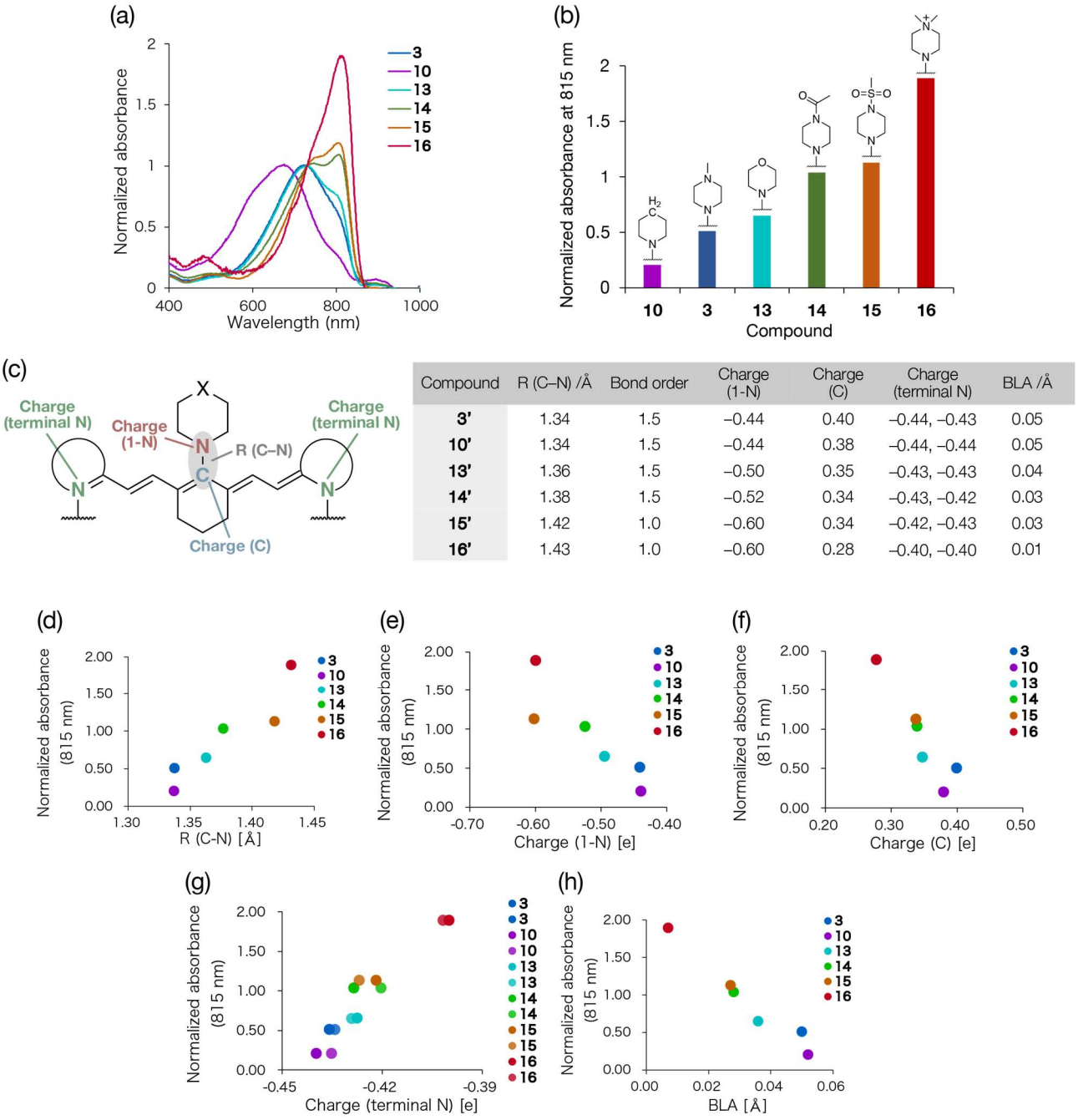

Compound	R (C–N) /Å	Bond order	Charge (1-N)	Charge (C)	Charge (terminal N)	BLA /Å
3'	1.34	1.5	–0.44	0.40	–0.44, –0.43	0.05
10'	1.34	1.5	–0.44	0.38	–0.44, –0.44	0.05
13'	1.36	1.5	–0.50	0.35	–0.43, –0.43	0.04
14'	1.38	1.5	–0.52	0.34	–0.43, –0.42	0.03
15'	1.42	1.0	–0.60	0.34	–0.42, –0.43	0.03
16'	1.43	1.0	–0.60	0.28	–0.40, –0.40	0.01

Figure 3. Investigation of the mechanism of pH-dependent absorption spectral changes. (a,b) Comparison of absorption peaks of dyes with various groups at position 4 in phosphate buffer at pH 7.0 containing 30% DMSO. The spectra were standardized based on the absorption peak intensities at 730 nm. Only the absorption spectrum of **3** was normalized by the absorbance at 680 nm due to a blue-shift in its spectrum. (c) Table summarizing C–N bond length, bond order, the charge of the N atom at position 1, and BLA for each dye. Graph plotting (d) charge of the N atom at position 1, (e) C–N bond length, (f) Charge (C), (g) Charge (terminal N), and (h) BLA versus normalized absorbance at 815 nm.

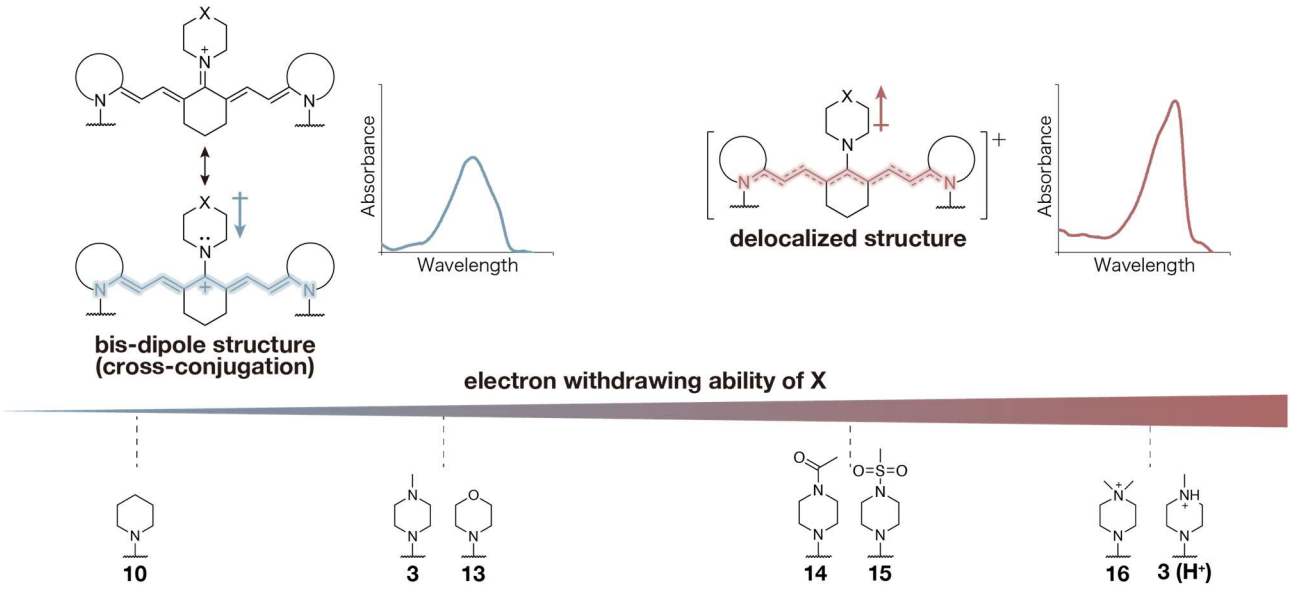

Figure 4. Electronic configuration of dyes bearing amino groups.

3.6. PA measurements of dyes bearing amino groups

To investigate whether the cyanine dyes can be applied for PA imaging, a dye with either a 1,4-diazaalkyl (**5**), 1,5-diazaalkyl (**7**), or 1-azaalkyl (**8**) group was dissolved in 0.01 M phosphate buffer containing 50% DMSO at pH 3.5 or 7.0, and the PA spectrum of each solution was measured by using a PA measurement setup (**Figure S2**). As shown in **Figure 5**, the PA spectra of all the cyanine dyes were largely correlated with their absorption spectra. Dye **5** exhibited significant pH-dependent changes in both PA signal and absorption spectra, suggesting its potential as a pH-responsive dye for PA imaging (**Figure 5a**).

To investigate the relationship between the PA signals and the optical properties of the dyes, the PA signals were plotted against absorbance, φ_f, and $\Delta\lambda$, and a correlation coefficient was calculated (**Figure S12**). The PA signals and absorbance showed a positive correlation with a correlation coefficient of 0.96 or higher for all dyes (**Figure S12a**). Dye **8** with a monoamino group showed high PA efficiency, whereas dyes **5** and **7**, with diazaalkyl groups, demonstrated equivalent PA efficiency regardless of the pH. When the peak values of the PA signals were plotted against φ_f of each dye, the correlation coefficient of dyes **5** and **7**, excluding dye **8** was –0.97, showing a negative correlation between the PA signal and φ_f (**Figure S12b**), while dye **7**, having a high φ_f, showed a high PA efficiency. The peak values of the PA signals were also plotted against $\Delta\lambda$, which could contribute to the generation of PA waves since large $\Delta\lambda$ generates heat derived from the vibrational relaxation of the dye to the S1 state. No correlation was, however, observed between the peak value of the PA signal and the Stokes shift (**Figure S12c**). The absence of a consistent relationship between the PA signal and φ_f or $\Delta\lambda$ may result from the complex non-radiative

processes in photo-excited molecules. The processes include vibrational relaxation, internal conversion, and intersystem crossing, which are complexly involved in the generating PA signals. At pH 7.0, dye **5** having a large Δλ, should not show a high PA efficiency compared to the other dyes due to its high φ_f. When the relationship between the wavelength of the excitation light and PA efficiency were investigated, excitation with light at shorter wavelengths resulted in higher PA efficiency (**Figure S13a**–**e**). This result suggests that the short-wavelength excitation increases the vibrational relaxation during the transition to the stable conformation of the excited state, resulting in an increase in the PA signal. (**Figure S13f**).

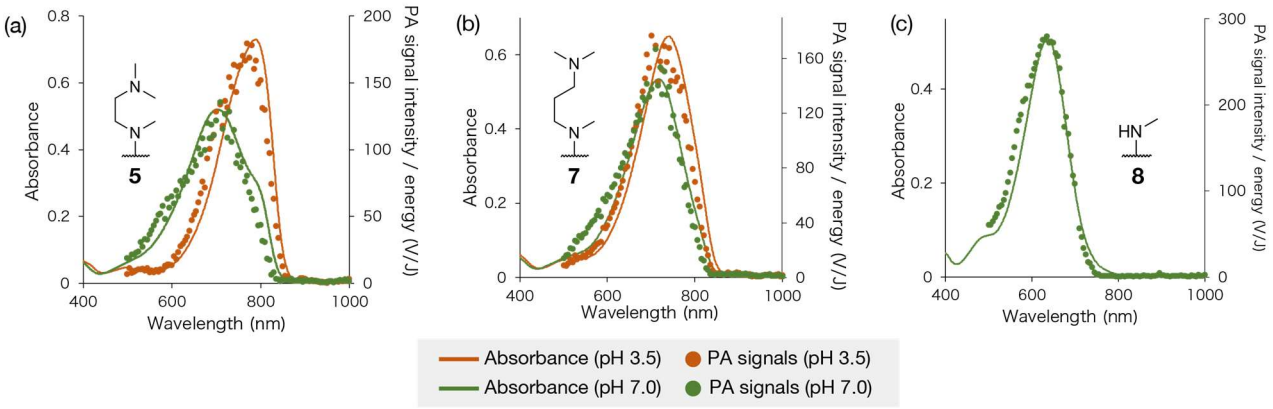

Figure 5. PA and absorption spectra of (a) **5**, (b) **7**, and (c) **8**. PA and absorption spectra were measured in 0.01 M phosphate buffer containing 50% DMSO at pH 3.5 (orange) and 7.0 (green). The final concentration of each dye was 10 μM.

3.7. Preparation of antibody-cyanine conjugates for cancer PA imaging

As exemplified by antibody-drug conjugates, antibodies are a powerful tool for delivering payloads to specific cells [29]. Therefore, we prepared antibody-cyanine conjugates for further evaluation in cancer cell PA imaging. To conjugate the pH responsive cyanine dye to an antibody, we designed and synthesized piperazine-based cyanine dyes with a carboxylate group **17**–**18** for binding a suitable antibody via an amide bond (**Scheme 2**). Besides piperazine-based dyes, we also designed and synthesized a piperidine-based dye, named **19**, which was used as control compound that does not exhibit pH responsiveness. To investigate the optical properties of **17**–**19**, the absorption and fluorescence spectra were measured in PB with 30% DMSO or DMSO (**Figures 6**, **S13**–**S15**). From the absorption and fluorescence spectra obtained, the optical properties of each compound were determined in the same manner as described above and are summarized in **Table 2**. The absorption and PA spectra of **17**–**18** changed when the pH diminished from neutral to acidic, whereas **19** showed no pH-dependent spectral changes (**Figures 6**, **S13**, **S16**), in agreement with the results obtained in **Figures 2** and **5**. When the relationship between PA signal

efficiency and optical properties were investigated, the PA signal intensities were positively correlated with absorbance in the same as **5**, **7**, and **8** (**Figure S18a**), but the PA signal efficiency at peaks were not correlated with φ_f (**Figure S18b**). The maxima of the PA spectra were positively correlated with Stokes shift, suggesting a significant contribution of vibrational relaxation for generating PA signals (**Figure S18c**). When the relationship between the wavelength of the excitation light and PA efficiency were investigated, excitation with light at shorter wavelengths resulted in higher PA efficiency in the same way as **5**, **7**, **8** (**Figure S19**). The p*K*a of **17**–**18** was 5.7 and 4.9, respectively, indicating that these dyes are suitable for PA imaging to detect weakly acidic conditions such as those occurring in lysosome [30], abnormal mitochondria [11], or tumor microenvironments [10] (**Figure S20**).

We also investigated stability of **17**–**19** under light exposure (**Figure 7**) or in the dark (**Figure S21**). After 60 minutes of light exposure, the residual absorbance of **17**–**19** at pH 7.0 with a 690 nm laser and **19** at pH 3.5 with a 690 nm laser were comparable to ICG (**Figure 7k**–**l**). On the other hand, the residual absorbance of **17**–**18** at pH 3.5 with a 785 nm laser were about 5 times higher than ICG (**Figure 7j**). The time to decrease by half of **17**–**18** was about three times longer than that of ICG (**Figure 7m**). ICG and **17**–**19** were then dissolved in PB with 30% DMSO and changes in absorption spectra in the dark were observed in time-course (**Figure S21**). **19** showed a slightly greater decrease in absorbance than ICG at pH 3.5 (**Figure S21i**), but under other conditions, **17**–**19** showed a similar or smaller decrease in absorbance than ICG, suggesting that the stability of **17**–**19** is comparable to that of ICG in the dark. (**Figure S21i**–**j**).

In addition, the cytotoxicity of **17**–**19** was also compared with ICG by propidium iodide (PI) staining (**Figure S22**). The percentage of dead cells with **17–19** was almost same as ICG, indicating that these dyes can be used for biological application.

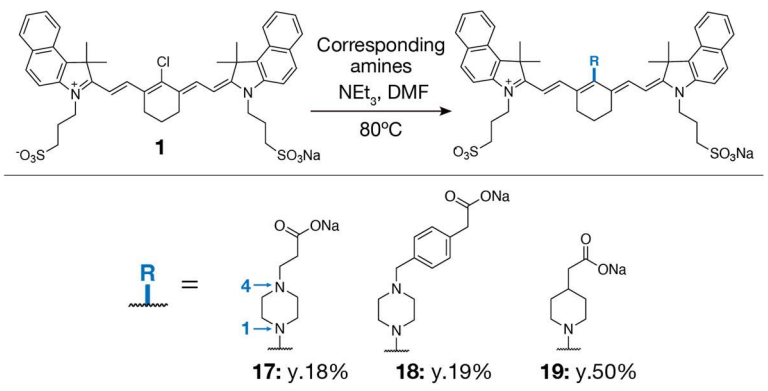

Scheme 2. Synthetic procedure and chemical structures of pH-responsive dyes.

Table 2. Optical properties of amine-substituted dyes at acidic and basic pH.

Compound	Abs_{max} (nm)[a]	Em_{max} (nm)[a]	Δλ (nm)[a]	ε ($M^{-1}cm^{-1}$)[a]	φ_f[b]	p*K*a[a]
17	720	828	108	6.8×10^4	0.12	-
17 ($+H^+$)	806	841	35	1.1×10^5	0.08	5.7
18	718	828	110	3.4×10^4	0.12	-
18 ($+H^+$)	802	842	40	5.0×10^4	0.08	4.9
19	683	823	140	5.2×10^4	0.13	-

a) phosphate buffer containing 30% DMSO, b) DMSO and DMSO with 1% TFA.

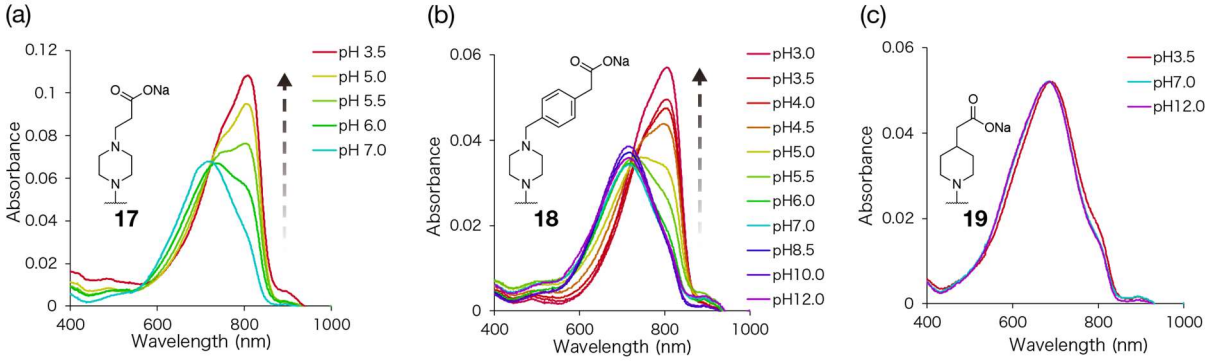

Figure 6. Absorption spectra of (a) **17**, (b) **18**, and (c) **19**. Absorption spectra were measured in a phosphate buffer containing 30% DMSO at pH 3.0–12.0. The final concentration of each dye was 1 μM.

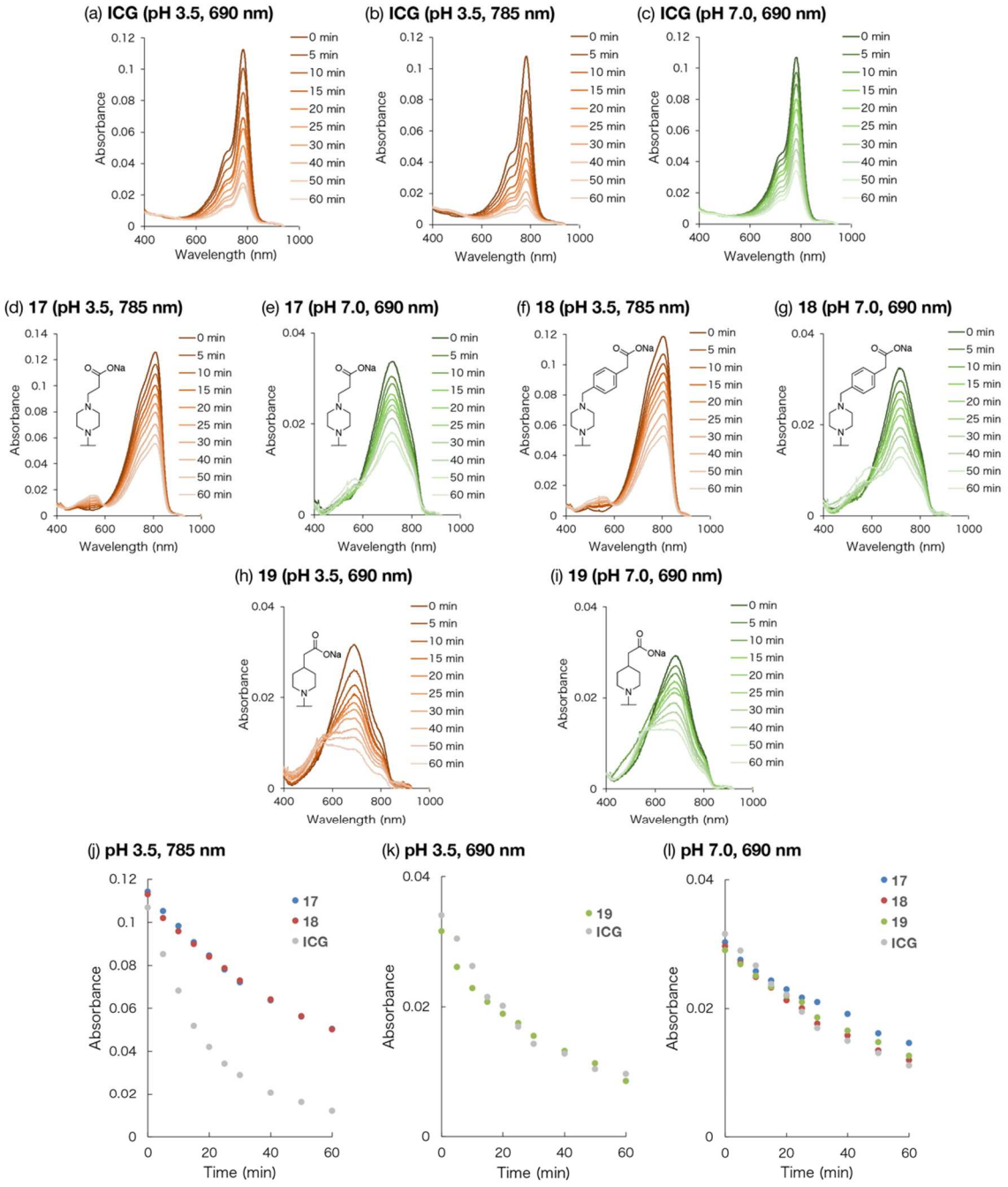

(m)

Compound	pH 3.5 (785 nm)	pH 3.5 (690 nm)	pH 7.0 (690 nm)
17	48.7 min	-	60.4 min
18	51.2 min	-	44.1 min
19	-	29.9 min	50.5 min
ICG	14.7 min	24.5 min	36.5 min

Figure 7. Absorption decays of 17–19 under light irradiation. Absorption decays were measured in a 0.1 M phosphate buffer with 30% DMSO at pH 3.5 and 7.0 in time-course. Each solution was irradiated by a 690 or 785 nm laser. (a–i) Absorption spectral changes monitored over a period of 60 minutes during light exposure. (j–l) Plots of absorption decays under light exposure. (m) Time required for the absorbance to decrease by half.

3.8. Evaluation of PA imaging agent accumulation in cultured cells by using a fluorescence microscope

To investigate whether **17**–**19** can be used for cancer cell imaging, the dyes were conjugated with the anti-EGFR

antibody panitumumab to afford **C1**–**C3** (**Scheme 3**). Then, we investigated whether these dyes could be specifically internalized in EGFR expressing HuCCT-1 cells by using fluorescence microscopy. After 24 h incubation of HuCCT-1 cells in the presence of each antibody-cyanine conjugate, the fluorescence of each dye could be observed from within the cells, implying that these conjugates were successfully internalized into the cells (**Figure 8a**). When the same observation was performed with EGFR non-expressing NIH-3T3 cells, after 24 h incubation with a dye, a very low fluorescence was observed compared to HuCCT-1 cells (**Figures 8b**, **S23**). These results suggested that each antibody-cyanine conjugate specifically accumulates in cancer cells by receptor-mediated endocytosis.

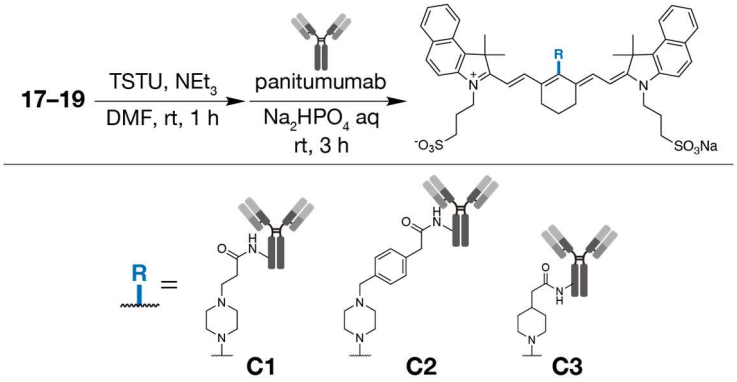

Scheme 3. Conjugation procedure of the dyes to an antibody.

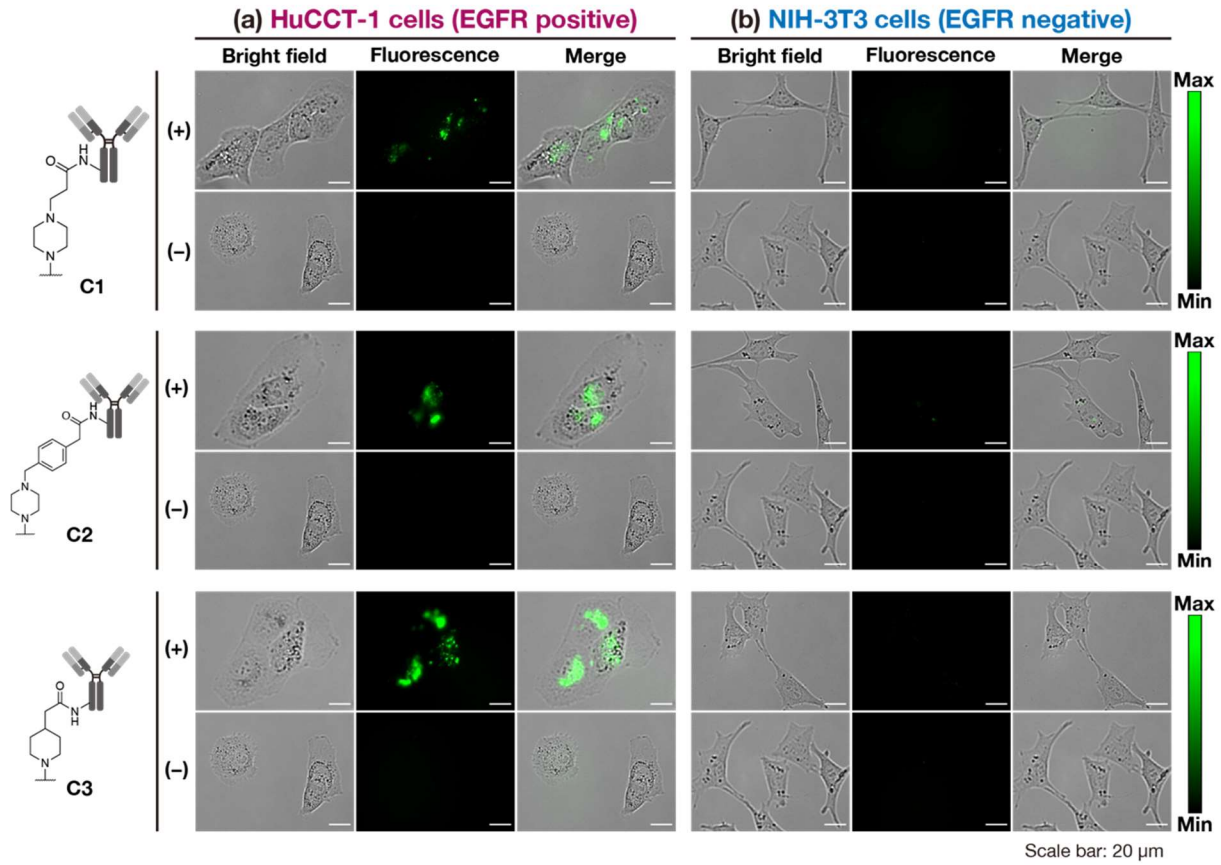

Figure 8. Fluorescence imaging of HuCCT-1 and NIH-3T3 cells with panitumumab-cyanine conjugates. Fluorescence of (a) EGFR high expressing HuCCT-1 and (b) EGFR low expressing NIH-3T3 cells was observed at 24 h after incubation with **C1**–**C3**, each at a final concentration of 5 μg/mL.

3.9. PA imaging of the cyanine dyes in cultured cancer cells

Next, to examine whether the PA signals may vary inside cancer cells, PA imaging upon excitation at 675 and 800 nm was performed using EGFR expressing MDA-MB-231 and HuCCT-1 cells with a PA microscope (**Figure S3**). Cell-seeded dish was soaked in water and PA signals were acquired from below the dish with an acoustic detector to avoid scattering of acoustic waves in the air. After incubating the cells with each antibody-cyanine conjugate for 24 h, PA signals were detected from the cells (**Figures 9**, **S24**). In cancer cells treated with **C1** and **C2**, the PA signals at 800 nm were stronger than those at 675 nm. On the other hand, PA signals at 675 nm was stronger than those at 800 nm in **C3**-treated cells (**Figure S25**). These results suggest that **C1** and **C2** changed the PA spectra in response to weakly acidic pH after accumulation in cancer cell lysosomes, supporting the notion that these conjugates could be promising candidates for high-contrast imaging of cancer cells. The PA intensities of **C1** and **C2** at 800 nm were not statistically different from those at 675 nm, but the conjugate bearing high p*K*a dye, **C1** tended to show higher PA intensities at 800 nm than **C2** (**Figures S25a**–**b**, **S25d**–**e**).

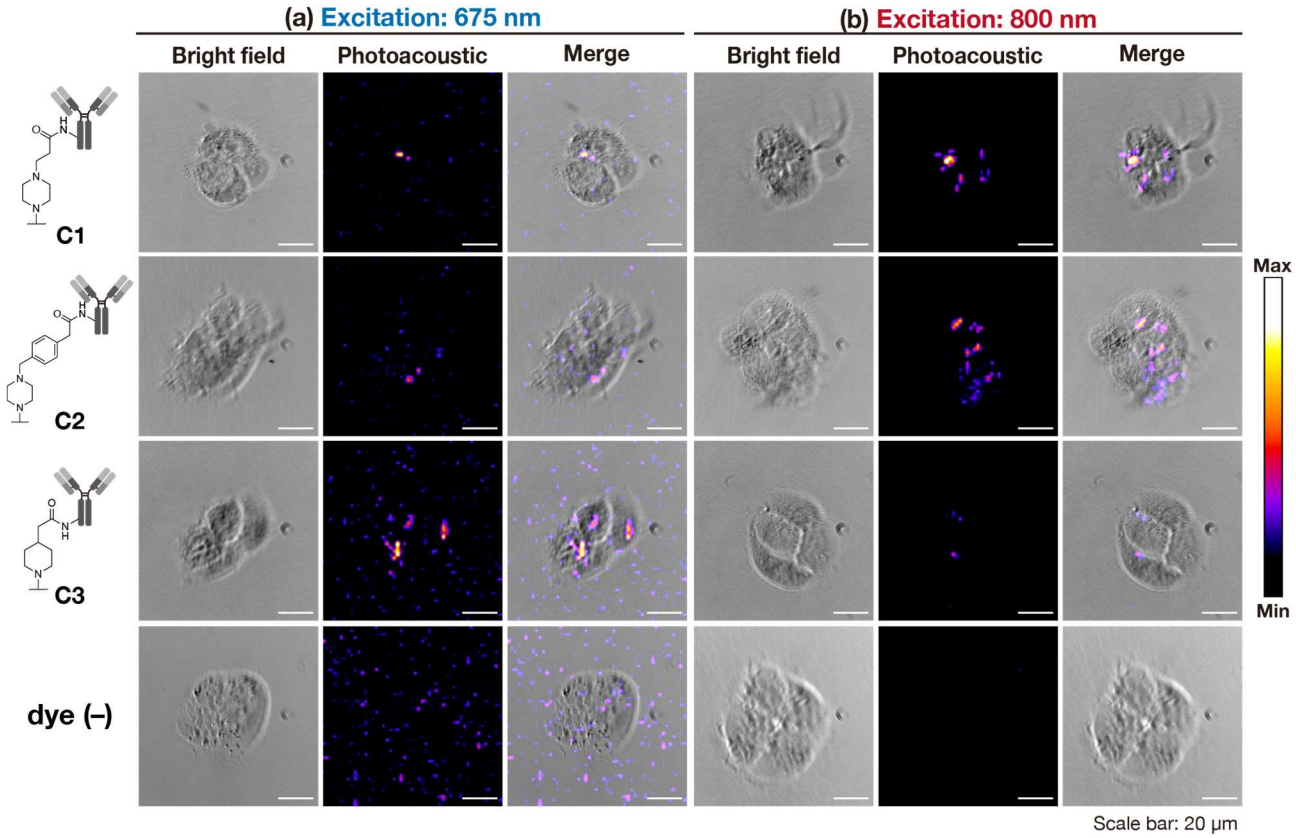

Figure 9. PA imaging of HuCCT-1 cells with pH responsive dye-antibody conjugates. HuCCT-1 cells were incubated with each dye-antibody conjugate for 24 h at 37ºC and then PA imaging was performed with nanosecond pulse light at (a) 675 nm and (b) 800 nm. Scale bar 20 μm.

4. Conclusion

PA imaging is a novel technique that overcomes the limitations of existing imaging methods due to its capacity to conveniently observe deep lesions, and it has been applied in several clinical contexts, particularly in thyroid [31,32] and breast [33–35] imaging with endogenous contrast agents such as hemoglobin. In addition, employing imaging agents could allow PA imaging to potentially depict lesions in a selective manner and high S/N ratio [36]. In this study, we reported novel and environmentally responsive cyanine dyes for cancer cell PA imaging. The imaging agent developed in this paper shows the first report of a pH-responsive antibody-dye conjugate for photoacoustic (PA) imaging. The absorption and PA spectra of the synthesized dyes changed in response to pH. The mechanism behind the spectral changes was revealed to involve the protonation of the amino group at position 4 of the piperazine moieties at acidic pH, with a consequential variation of the electron withdrawing ability of the amino group and decreased contribution of bis-dipole form. When the pH-responsive dyes conjugated with a cancer-specific antibody were added to cancer cells, PA signals due to the lysosome acidic pH were detected from cancer

cells. Based on these findings, the proposed pH-responsive cyanine dyes have the potential to be employed for detecting EGFR expressing cancer at high S/N ratios. By using other types of antibodies, such as HER2-targeting Trastuzumab or CD30-targeting Brentuximab, these dyes would have potential to detect various cancer subtypes [37]. Additionally, the pH-responsive dye changes the ratio of its absorption spectrum before and after protonation. As a future application, ratiometric imaging of tumors can be performed, allowing for the detection of lesions independent of dye concentration. On the other hand, an unprecedented mechanism was revealed for these pH-responsive dyes and can be expected to be exploited for the development of PA imaging agents for the detection of various biomolecules or enzymes such as tumor-associated proteases. In the future, the herein delineated piperazine-based mechanism may contribute to the development of diagnostic imaging agents.

AUTHOR INFORMATION

Corresponding Author

***Mikako Ogawa** – Laboratory of Bioanalysis and Molecular Imaging, Graduate School of Pharmaceutical Sciences, Hokkaido University, Sapporo, Hokkaido 060-0812, Japan

Phone: +81-11-706-3767, Fax: +81-11-706-3767.

E-mail: mogawa@pharm.hokudai.ac.jp

Notes

The authors declare no competing financial interest.

ACKNOWLEDGMENT

This work was supported by JST SPRING (Grant Number JPMJSP2119), JSPS KAKENHI (Grant Numbers JP18H04723 “Resonance Bio” and JP22K06544), AMED (Grant Numbers JP21zf0127004 and JP19am0101093), the Photo-excitonix Project at Hokkaido University, and MEXT (Grant Number JPMXS0420100120). We thank the Instrumental Analysis Division, Global Facility Center, Creative Research Institution, Hokkaido University, for ESI-MS Exactive Mass Spectrometer assistance and their insight and expertise that greatly contributed to this study.

ASSOCIATED CONTENT

Supporting Information

Additional experimental data, which includes general information on the experimental equipment, additional methods, the synthetic procedure for compounds **S1**–**S7**, and supplementary figures (PDF).

REFERENCE

[1] B.A. Webb, M. Chimenti, M.P. Jacobson, D.L. Barber, Dysregulated pH: a perfect storm for cancer progression, Nat. Rev. Cancer 11 (2011) 671–677. https://doi.org/10.1038/nrc3110.

[2] A. Steinegger, O.S. Wolfbeis, S.M. Borisov, Optical Sensing and Imaging of pH Values: Spectroscopies, Materials, and Applications, Chem. Rev. 120 (2020) 12357–12489. https://doi.org/10.1021/acs.chemrev.0c00451.

[3] J.-T. Hou, W.X. Ren, K. Li, J. Seo, A. Sharma, X.-Q. Yu, J.S. Kim, Fluorescent bioimaging of pH: from design to applications, Chem. Soc. Rev. 46 (2017) 2076–2090. https://doi.org/10.1039/c6cs00719h.

[4] H. Lee, W. Akers, K. Bhushan, S. Bloch, G. Sudlow, R. Tang, S. Achilefu, Near-Infrared pH-Activatable Fluorescent Probes for Imaging Primary and Metastatic Breast Tumors, Bioconjugate Chem. 22 (2011) 777–784. https://doi.org/10.1021/bc100584d.

[5] H. Fujioka, S. Uno, M. Kamiya, R. Kojima, K. Johnsson, Y. Urano, Activatable fluorescent probes for hydrolase enzymes based on coumarin–hemicyanine hybrid fluorophores with large Stokes shifts, Chem. Commun. 56 (2020) 5617–5620. https://doi.org/10.1039/d0cc00559b.

[6] L.V. Wang, S. Hu, Photoacoustic Tomography: In Vivo Imaging from Organelles to Organs, Science 335 (2012) 1458–1462. https://doi.org/10.1126/science.1216210.

[7] C. Li, T.R. Greenwood, Z.M. Bhujwalla, K. Glunde, Synthesis and Characterization of Glucosamine-Bound Near-Infrared Probes for Optical Imaging, Org. Lett. 8 (2006) 3623–3626. https://doi.org/10.1021/ol060783e.

[8] S. Guha, G.K. Shaw, T.M. Mitcham, R.R. Bouchard, B.D. Smith, Croconaine rotaxane for acid activated photothermal heating and ratiometric photoacoustic imaging of acidic pH, Chem. Commun. 52 (2016) 120–123. https://doi.org/10.1039/c5cc08317f.

[9] H. Mu, K. Miki, H. Harada, K. Tanaka, K. Nogita, K. Ohe, pH-Activatable Cyanine Dyes for Selective Tumor Imaging Using Near-Infrared Fluorescence and Photoacoustic Modalities, ACS Sens. 6 (2021) 123–129. https://doi.org/10.1021/acssensors.0c01926.

[10] S. Takahashi, Y. Kagami, K. Hanaoka, T. Terai, T. Komatsu, T. Ueno, M. Uchiyama, I. Koyama-Honda, N. Mizushima, T. Taguchi, H. Arai, T. Nagano, Y. Urano, Development of a Series of Practical Fluorescent Chemical Tools To Measure pH Values in Living Samples, J. Am. Chem. Soc. 140 (2018) 5925–5933. https://doi.org/10.1021/jacs.8b00277.

[11] M.H. Lee, N. Park, C. Yi, J.H. Han, J.H. Hong, K.P. Kim, D.H. Kang, J.L. Sessler, C. Kang, J.S. Kim, Mitochondria-Immobilized pH-Sensitive Off–On Fluorescent Probe, J. Am. Chem. Soc. 136 (2014) 14136–14142. https://doi.org/10.1021/ja506301n.

[12] T. Myochin, K. Kiyose, K. Hanaoka, H. Kojima, T. Terai, T. Nagano, Rational Design of Ratiometric Near-Infrared Fluorescent pH Probes with Various pK a Values, Based on Aminocyanine, J. Am. Chem. Soc. 133 (2011) 3401–3409. https://doi.org/10.1021/ja1063058.

[13] A. Azhdarinia, N. Wilganowski, H. Robinson, P. Ghosh, S. Kwon, Z.W. Lazard, A.R. Davis, E. Olmsted-Davis, E.M. Sevick-Muraca, Characterization of chemical, radiochemical and optical properties of a dual-labeled MMP-9 targeting peptide, Bioorg. Med. Chem. 19 (2011) 3769–3776. https://doi.org/10.1016/j.bmc.2011.04.054.

[14] S. Pascal, A. Haefele, C. Monnereau, A. Charaf-Eddin, D. Jacquemin, B.L. Guennic, C. Andraud, O. Maury, Expanding the Polymethine Paradigm: Evidence for the Contribution of a Bis-Dipolar Electronic Structure, J. Phys. Chem. A 118 (2014) 4038–4047. https://doi.org/10.1021/jp501358q.

[15] S.G. König, R. Krämer, Accessing Structurally Diverse Near-Infrared Cyanine Dyes for Folate Receptor-Targeted Cancer Cell Staining, 23 (2017). https://doi.org/10.1002/chem.201700026.

[16] T. Hirasawa, R.J. Iwatate, M. Kamiya, S. Okawa, Y. Urano, M. Ishihara, Multispectral photoacoustic imaging of tumours in mice injected with an enzyme-activatable photoacoustic probe, J. Opt. 19 (2016) 014002. https://doi.org/10.1088/2040-8978/19/1/014002.

[17] N. Narayanan, G. Patonay, A New Method for the Synthesis of Heptamethine Cyanine Dyes: Synthesis of New Near-Infrared Fluorescent Labels, J. Org. Chem. 60 (1995) 2391–2395. https://doi.org/10.1021/jo00113a018.

[18] G.O. Menéndez, M.E. Pichel, C.C. Spagnuolo, E.A. Jares-Erijman, NIR fluorescent biotinylated cyanine dye: optical properties and combination with quantum dots as a potential sensing device, Photochem. Photobiol. Sci. 12 (2013) 236–240. https://doi.org/10.1039/c2pp25174d.

[19] J.L. Bricks, Y.L. Slominskii, I.D. Panas, A.P. Demchenko, Fluorescent J-aggregates of cyanine dyes: basic research and applications review, Methods Appl. Fluoresc. 6 (2017) 012001. https://doi.org/10.1088/2050-6120/aa8d0d.

[20] A. Mishra, R.K. Behera, P.K. Behera, B.K. Mishra, G.B. Behera, Cyanines during the 1990s: A Review, Chem. Rev. 100 (2000) 1973–2012. https://doi.org/10.1021/cr990402t.

[21] F. Würthner, T.E. Kaiser, C.R. Saha-Möller, J-Aggregates: From Serendipitous Discovery to Supramolecular Engineering of Functional Dye Materials, Angew. Chem. Int. Ed. 50 (2011) 3376–3410. https://doi.org/10.1002/anie.201002307.

[22] SciFinder-n: Calculated using Advanced Chemistry Development (ACD/Labs) Software V11.02 (© 1994-2023 ACD/Labs), n.d.

[23] F. Meyers, S.R. Marder, B.M. Pierce, J.L. Bredas, Electric Field Modulated Nonlinear Optical Properties of Donor-Acceptor Polyenes: Sum-Over-States Investigation of the Relationship between Molecular Polarizabilities (.alpha., .beta., and .gamma.) and Bond Length Alternation, J. Am. Chem. Soc. 116 (1994) 10703–10714. https://doi.org/10.1021/ja00102a040.

[24] H. Hu, O.V. Przhonska, F. Terenziani, A. Painelli, D. Fishman, T.R. Ensley, M. Reichert, S. Webster, J.L. Bricks, A.D. Kachkovski, D.J. Hagan, E.W.V. Stryland, Two- photon absorption spectra of a near-infrared 2-azaazulene polymethine dye: solvation and ground-state symmetry breaking, Phys. Chem. Chem. Phys. 15 (2013) 7666–7678. https://doi.org/10.1039/c3cp50811k.

[25] S. Pascal, S. Chi, J.W. Perry, C. Andraud, O. Maury, Impact of Ion-Pairing Effects on Linear and Nonlinear Photophysical Properties of Polymethine Dyes, ChemPhysChem 21 (2020) 2536–2542. https://doi.org/10.1002/cphc.202000731.

[26] A. Kurutos, Y. Shindo, Y. Hiruta, K. Oka, D. Citterio, Near-infrared pH responsive heptamethine cyanine platforms: Modulating the proton acceptor, Dyes Pigments 181 (2020) 108611. https://doi.org/10.1016/j.dyepig.2020.108611.

[27] H.E. Katz, Hydride sponge: 1,8-naphthalenediylbis(dimethylborane), J. Am. Chem. Soc. 107 (1985) 1420–1421. https://doi.org/10.1021/ja00291a057.

[28] R.W. Alder, P.S. Bowman, W.R.S. Steele, D.R. Winterman, The remarkable basicity of 1,8-bis(dimethylamino)naphthalene, Chem. Commun. (Lond.) 0 (1968) 723–724. https://doi.org/10.1039/c19680000723.

[29] A. Beck, L. Goetsch, C. Dumontet, N. Corvaïa, Strategies and challenges for the next generation of antibody–drug conjugates, Nat. Rev. Drug Discov. 16 (2017) 315–337. https://doi.org/10.1038/nrd.2016.268.

[30] J. Zhang, M. Yang, C. Li, N. Dorh, F. Xie, F.-T. Luo, A. Tiwari, H. Liu, Near-infrared fluorescent probes based on piperazine-functionalized BODIPY dyes for sensitive detection of lysosomal pH, J. Mater. Chem. B 3 (2015) 2173–2184. https://doi.org/10.1039/c4tb01878h.

[31] A. Dima, V. Ntziachristos, In-vivo handheld optoacoustic tomography of the human thyroid, Photoacoustics 4 (2016) 65–69. https://doi.org/10.1016/j.pacs.2016.05.003.

[32] M. Yang, L. Zhao, X. He, N. Su, C. Zhao, H. Tang, T. Hong, W. Li, F. Yang, L. Lin, B. Zhang, R. Zhang, Y. Jiang, C. Li, Photoacoustic/ultrasound dual imaging of human thyroid cancers: an initial clinical study, Biomed. Opt. Express 8 (2017) 3449–3457. https://doi.org/10.1364/boe.8.003449.

[33] E.I. Neuschler, R. Butler, C.A. Young, L.D. Barke, M.L. Bertrand, M. Böhm-Vélez, S. Destounis, P. Donlan, S.R. Grobmyer, J. Katzen, K.A. Kist, P.T. Lavin, E.V. Makariou, T.M. Parris, K.J. Schilling, F.L. Tucker, B.E. Dogan, A Pivotal Study of Optoacoustic Imaging to Diagnose Benign and Malignant Breast Masses: A New Evaluation Tool for Radiologists, Radiology 287 (2018) 398–412. https://doi.org/10.1148/radiol.2017172228.

[34] G. Diot, S. Metz, A. Noske, E. Liapis, B. Schroeder, S.V. Ovsepian, R. Meier, E. Rummeny, V. Ntziachristos, Multispectral Optoacoustic Tomography (MSOT) of Human Breast Cancer, Clin. Cancer Res. 23 (2017) 6912–6922. https://doi.org/10.1158/1078-0432.ccr-16-3200.

[35] M. Toi, Y. Asao, Y. Matsumoto, H. Sekiguchi, A. Yoshikawa, M. Takada, M. Kataoka, T. Endo, N. Kawaguchi-Sakita, M. Kawashima, E. Fakhrejahani, S. Kanao, I. Yamaga, Y. Nakayama, M. Tokiwa, M. Torii, T. Yagi, T. Sakurai, K. Togashi, T. Shiina, Visualization of tumor-related blood vessels in human breast by photoacoustic imaging system with a hemispherical detector array, Sci Rep-Uk 7 (2017) 41970. https://doi.org/10.1038/srep41970.

[36] M.Y. Lucero, Y. Tang, C.J. Zhang, S. Su, J.A. Forzano, V. Garcia, X. Huang, D. Moreno, J. Chan, Activity-based photoacoustic probe for biopsy-free assessment of copper in murine models of Wilson's disease and liver metastasis, Proc. Natl. Acad. Sci. 118 (2021) e2106943118. https://doi.org/10.1073/pnas.2106943118.

[37] M. Ogawa, C.A.S. Regino, P.L. Choyke, H. Kobayashi, In vivo target-specific activatable near-infrared optical labeling of humanized monoclonal antibodies, Mol. Cancer Ther. 8 (2009) 232–239. https://doi.org/10.1158/1535-7163.mct-08-0862.